Heavy-ion collisions — selected topics

U.A. Wiedemann
CERN, Geneva, Switzerland

Abstract
We discuss selected topics of the theory of heavy-ion collisions.

1 Introduction

How do complex, collective phenomena and properties of matter emerge from the fundamental interactions between elementary particles? Heavy-ion physics addresses this question for the theory of strong interactions, Quantum Chromodynamics, in the regime of extreme energy density.

For idealized situations, such as perfect thermal equilibrium, QCD allows us to calculate the equation of state of strongly interacting matter, the thermodynamic and dissipative properties which govern the propagation of disturbances in that matter, the fate of non-equilibrated structures such as bound states or jets embedded in that matter, the electromagnetic radiation from that matter, etc. An introductory text to heavy-ion physics could start by explaining the calculational techniques and main results of QCD thermodynamics and non-equilibrium dynamics, before focusing on those measurements which are regarded as most suited for a test of QCD at extreme temperature or energy density. A byproduct of such a presentation would be that the text stays close to the historical development of the subject and that it would recall naturally the main motivations for studying nucleus–nucleus collisions.

However, such a presentation poses also the risk — in particular for the novice in the field — of approaching the rich phenomenology of heavy-ion physics with the unwanted bias of a preconceived theoretical framework. Collective phenomena are not simply there in the data, they need to be established on top of a non-trivial background. And where collective phenomena can be established, they are not necessarily of thermal origin. Moreover, analysis and interpretation of data often require modelling as a bridge between experimental observations and QCD. This multi-step process is at best as reliable as its weakest link. Hence to contribute to research in the field, knowledge about the steps from the first data to a final interpretation appears to be at least as important as the knowledge about the theory of QCD thermodynamics. This motivates our presentation.

The following lectures aim at an introduction to the methods used in heavy-ion physics for establishing collective phenomena and for analysing them in the framework of Quantum Chromodynamics. To the extent possible, our discussion will follow for each class of measurements a three-step logic.

1. Establish benchmarks in which collective effects are absent.
2. Quantify deviations from these benchmarks.
3. Analyse the origin of these deviations.

We introduce different classes of measurements roughly in the order in which they become experimentally accessible in collider experiments. The limited scope of these lectures allows me to touch only a few prominent examples.

2 Multiplicity distributions

Figure 1 shows one of the very first measurements at a heavy-ion collider: the number of collisions N_{ev} (‘events’) recorded by an experiment, is plotted as a function of the event multiplicity n. In contrast to proton–proton collisions, this distribution shows for heavy-ion collisions a prolonged tail towards higher multiplicity.

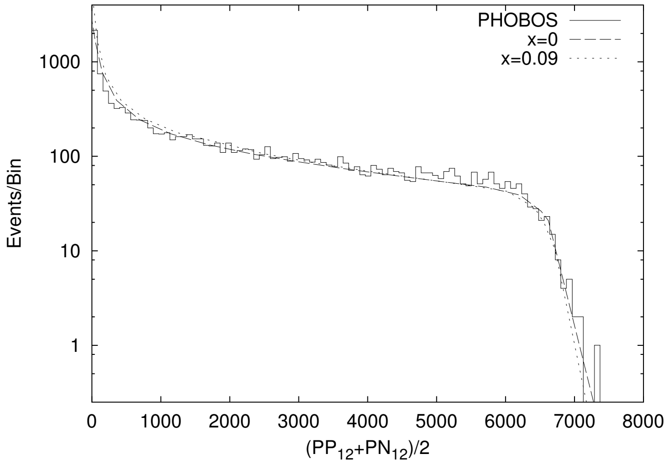

Fig. 1: One of the first measurements at the Relativistic Heavy Ion Collider RHIC: The number of collisions ('events') registered by PHOBOS, plotted versus a signal strength, is proportional to the event multiplicity. Figure taken from Ref. [1], curves discussed in the text of Section 2.2.

We want to establish a benchmark for $dN_{\rm ev}/dn$, in which collective effects are absent. To this end, we want to determine the multiplicity distribution $dN_{\rm ev}/dn$ under the assumption that particle production in $A+B$ is an incoherent superposition of the collision of an *equivalent* number of nucleon–nucleon collisions. The notion of an 'equivalent number' requires a counting rule. In Glauber theory, this counting is based on the number of participants $N_{\rm part}$, which is the number of nucleons in A and B, which participate in the collision, or it is based on the total number of nucleon–nucleon collisions $N_{\rm coll}$ which occur in the collision of A with B. However, there is no a priori reason for not choosing another counting rule, based, for example, on the number of valence quarks rather than nucleons in A and B.

How can we hope to arrive at firm conclusions if the very starting point depends on such an ambiguous choice of what we count? The answer is that the shape of the multiplicity distribution $dN_{\rm ev}/dn$ is rather insensitive to the mechanism of multiparticle production. It is determined largely by purely geometrical information about the overlap of A and B as a function of impact parameter. As a consequence, the shape of $dN_{\rm ev}/dn$ is not useful for determining collective phenomena, but it is a powerful tool for characterizing the geometry of the collision. To determine the latter, it does not matter so much what we count, but it matters that we count. This section gives arguments of why this is so, and it outlines in technical detail how one usually proceeds. And as we shall see in subsequent sections, looking at other measurements as a function of geometrical information about the collision can discriminate collective phenomena from an underlying background.

2.1 Glauber theory

The distribution of nucleons in a nucleus A is characterized by the nuclear density $\rho_A(\vec{r})$. This density depends on the 3-dimensional radius $\vec{r}$. We set its norm to unity, $\int d\vec{r}\,\rho_A(\vec{r}) = 1$. At high centre-of-mass energies, the spherical nucleus is Lorentz-contracted along the beam direction z and what matters is the projection of the nuclear density on the plane of transverse impact parameter b. This transverse density is given by the nuclear profile function

$$T_A(\mathbf{b}) = \int_{-\infty}^{\infty} dz\,\rho(\mathbf{b},z)\,. \tag{1}$$

The nucleon–nucleon interaction can be characterized by its inelastic cross section $\sigma_{\rm nn}^{\rm inel}$, which we write differential in impact parameter, $\int d\mathbf{r}\,\sigma(\mathbf{r}) = \sigma_{\rm nn}^{\rm inel}$. We now discuss nucleon–nucleus (n–A) and nucleus–nucleus (A–B) collisions as incoherent superpositions of nucleon–nucleon collisions.

2.1.1 Nucleon–nucleus (n–A) collisions

For an n–A collision at impact parameter $\mathbf{b}$, the probability that the projectile nucleon n interacts with the i'th target nucleon at transverse position $\mathbf{s}_i^A$, $i \in [1, A]$, is

$$p(\mathbf{b}, i) = \int d\mathbf{s}_i^A \, T_A(\mathbf{s}_i^A) \, \sigma(\mathbf{b} - \mathbf{s}_i^A) \simeq T_A(\mathbf{b}) \, \sigma_{\mathrm{nn}}^{\mathrm{inel}} \,. \tag{2}$$

Here, $T_A(\mathbf{b})$ is the number of nucleons at impact parameter $\mathbf{b}$. We assumed in the second step of (2) that the n–n cross section is very small compared to the transverse area of the nucleus, and that the differential cross section can be written as

$$\sigma(\mathbf{b} - \mathbf{s}) \simeq \sigma_{\mathrm{nn}}^{\mathrm{inel}} \, \delta^{(2)}(\mathbf{b} - \mathbf{s}) \,. \tag{3}$$

We shall adopt this approximation throughout our discussion. The one-interaction probability (2) is independent of the index i, $p(\mathbf{b}, i) = p(\mathbf{b})$. It determines the probability $P(n, \mathbf{b})$ that the nucleon undergoes exactly n interactions with nucleons inside A,

$$P(n, \mathbf{b}) = \begin{pmatrix} A \\ n \end{pmatrix} [1 - p(\mathbf{b})]^{A-n} \, p(\mathbf{b})^n \,. \tag{4}$$

From this one calculates the average number of nucleon–nucleon collisions in an n–A collision at impact parameter $\mathbf{b}$,

$$\overline{N}_{\mathrm{coll}}^{nA}(\mathbf{b}) = \sum_{n=0}^{A} n \, P(n, \mathbf{b}) = A \, T_A(\mathbf{b}) \, \sigma_{\mathrm{nn}}^{\mathrm{inel}} \,. \tag{5}$$

In n–A collisions, the number of collisions is always one less than the number of nucleons participating in the collisions, so

$$\overline{N}_{\mathrm{part}}^{nA}(\mathbf{b}) = 1 + \overline{N}_{\mathrm{coll}}^{nA}(\mathbf{b}) \,. \tag{6}$$

We spell this out since it will be different in A–B collisions. The inelastic n–A cross section $\sigma_{\mathrm{nA}}^{\mathrm{inel}}$ is given by the probability $[1 - P(0, \mathbf{b})]$ that some interaction occurs at impact parameter $\mathbf{b}$, integrated over impact parameter,

$$\sigma_{\mathrm{nA}}^{\mathrm{inel}} \;\equiv\; \int d\mathbf{b} \, [1 - P_0(\mathbf{b})] \simeq \int d\mathbf{b} \left[1 - \left[1 - T_A(\mathbf{b}) \, \sigma_{\mathrm{nn}}^{\mathrm{inel}} \right]^A \right] \,. \tag{7}$$

In the so-called optical limit, $A \gg 1$, we can exponentiate the integrand,

$$\sigma_A(\mathbf{b}) = \left[1 - \left[1 - T_A(\mathbf{b}) \, \sigma_{\mathrm{nn}}^{\mathrm{inel}} \right]^A \right] \simeq \left[1 - \exp\left[-A \, T_A(\mathbf{b}) \, \sigma_{\mathrm{nn}}^{\mathrm{inel}} \right] \right] \,. \tag{8}$$

2.1.2 Nucleus–nucleus (A–B) collisions

In an A–B collision at impact parameter $\mathbf{b}$, a nucleon at transverse position $\mathbf{s}^B$ in nucleus B will undergo on average $\overline{N}_{\mathrm{coll}}^{nA}(\mathbf{b} - \mathbf{s}^B) = A \, T_A(\mathbf{b} - \mathbf{s}^B) \, \sigma_{\mathrm{nn}}^{\mathrm{inel}}$ collisions, see Eq. (5). So, the average number of nucleon–nucleon collisions in A–B at impact parameter $\mathbf{b}$ is

$$\overline{N}_{\mathrm{coll}}^{AB}(\mathbf{b}) = B \int d\mathbf{s}^B \, T_B(\mathbf{s}^B) \, \overline{N}_{\mathrm{coll}}^{nA}(\mathbf{b} - \mathbf{s}^B) = A \, B \, T_{AB}(\mathbf{b}) \, \sigma_{\mathrm{nn}}^{\mathrm{inel}} \,. \tag{9}$$

Here, we encounter for the first time the nuclear overlap function

$$T_{AB}(\mathbf{b}) \equiv \int d\mathbf{s} \, T_B(\mathbf{s}) \, T_A(\mathbf{b} - \mathbf{s}) \,, \tag{10}$$

which plays a central role in describing the transverse geometry of heavy-ion collisions. Other quantities of interest can be calculated by starting with the probability that a nucleon at position $\mathbf{s}^B$ in B participates in the collision. If the nucleons in A are in the configuration $\{\mathbf{s}_i^A\}$, then the probability that the j-th nucleon at position $\mathbf{s}_j^B$ in B interacts with at least one nucleon in A is

$$p(\mathbf{s}_j^B, \{\mathbf{s}_i^A\}) = 1 - \prod_{i=1}^{A} \left[1 - \sigma(\mathbf{s}^B - \mathbf{s}_i^A)\right] \,. \tag{11}$$

The probability for nucleons in an arbitrary configuration $\{\mathbf{s}_i^A\}$ that in the collision of B with A at impact parameter b exactly m nucleons of B participate and $(B-m)$ do not is

$$\begin{aligned} P_B(m, \mathbf{b}) = \left(\begin{array}{c} B \\ m \end{array} \right) & \left(\prod_{i=1}^{A} \prod_{j=1}^{B} \int d\mathbf{s}_i^A \, d\mathbf{s}_j^B \, T_A(\mathbf{s}_i^A) \, T_B(\mathbf{s}_j^B - \mathbf{b}) \right) \\ & \times p(\mathbf{s}_1^B, \{\mathbf{s}_i^A\}) \dots p(\mathbf{s}_m^B, \{\mathbf{s}_i^A\}) \left[1 - p(\mathbf{s}_{m+1}^B, \{\mathbf{s}_i^A\})\right] \dots \left[1 - p(\mathbf{s}_B^B, \{\mathbf{s}_i^A\})\right] \,. \end{aligned} \tag{12}$$

From this, many other quantities of interest can be calculated in a straightforward way (see Question 1 below). For instance, the inelastic cross section is defined by the probability that something happens at impact parameter $\mathbf{b}$, integrated over impact parameter

$$\sigma_{AB}^{\text{inel}} \equiv \int d\mathbf{b} \, \left[1 - P_B(0, \mathbf{b})\right] = \int d\mathbf{b} \, \left[1 - \left[1 - T_{AB}(\mathbf{b}) \, \sigma_{\text{nn}}^{\text{inel}}\right]^{AB}\right] \,. \tag{13}$$

We can invoke the optical limit $AB \gg 1$ to exponentiate the integrand

$$\sigma_{AB}(\mathbf{b}) = \left[1 - P_B(0, \mathbf{b})\right] \simeq 1 - \exp\left[-A\, B\, T_{AB}(\mathbf{b}) \, \sigma_{\text{nn}}^{\text{inel}}\right] \,. \tag{14}$$

We find that for the inelastic cross section as well as for the average number of collisions, the nuclear overlap function plays the role which the nuclear profile function played for n–A collisions; more precisely, the expressions for n–A and A–B collisions are related by the substitution $A\, T_A \to A\, B\, T_{AB}$. The situation is different for the average number of participants. The average number of nucleons in B participating in an A–B collision at impact parameter b is

$$\frac{1}{1 - P_B(0, \mathbf{b})} \sum_{m=1}^{B} m \, P_B(0, \mathbf{b}) = \frac{B \, \sigma_A(\mathbf{b})}{1 - P_B(0, \mathbf{b})} \,. \tag{15}$$

Here, the denominator keeps count of the fact that only those encounters of A with B are registered, in which something is happening. The average number of participating nucleons in A and B is obtained by symmetrizing this expression

$$\overline{N}_{\text{part}}^{AB}(\mathbf{b}) = \frac{B \, \sigma_A(\mathbf{b})}{\sigma_{AB}(\mathbf{b})} + \frac{A \, \sigma_B(\mathbf{b})}{\sigma_{AB}(\mathbf{b})} \,. \tag{16}$$

Parametrically, the average number of participants in A–A grows proportional to A, the average number of collisions grows proportional to $A^{4/3}$ (see Question 2 below for a simple example).

To turn the above equations into numbers, we have to specify the nuclear density $\rho(\mathbf{r})$ and the inelastic nucleon–nucleon cross section σ_{NN}. For the nuclear density of sufficiently large nuclei, $A > 16$, one commonly uses the Woods–Saxon parametrization

$$\rho(\mathbf{r}) = \rho_0 \, \frac{1}{\left(1 + \exp\left[-\frac{r-R}{c}\right]\right)} \,, \qquad R = 1.07 \, A^{1/3} \, \text{fm} \,, \qquad c = 0.545 \, \text{fm} \,. \tag{17}$$

More precise parametrizations can be found for instance in Ref. [2]. The inelastic nucleon–nucleon cross section is $\sigma_{\text{nn}}^{\text{inel}} \sim 40$ mb at $\sqrt{s} \sim 100$ GeV.

Questions:

1. Derive Eqs. (13) and (15), starting from Eq. (12).
   Answer: In terms of the shorthand $\overline{p}(\mathbf{b},\{\mathbf{s}_i^A\}) \equiv \int d\mathbf{s}_j^B\, T_B(\mathbf{s}_j^B-\mathbf{b})\, p(\mathbf{s}_j^B,\{\mathbf{s}_i^A\})$, the probability $P_B(m,\mathbf{b})$ of Eq. (12) reads
   $$P_B(m,\mathbf{b}) = \left(\prod_{i=1}^{A} \int d\mathbf{s}_i^A\, T_A(\mathbf{s}_i^A)\right) \begin{pmatrix} B\\ m\end{pmatrix} \overline{p}(\mathbf{b},\{\mathbf{s}_i^A\})^m \left[1-\overline{p}(\mathbf{b},\{\mathbf{s}_i^A\})\right]^{B-m} .$$
   Using $\sum_{m=0}^{B} m \begin{pmatrix}B\\ m\end{pmatrix} \overline{p}^m \, [1-\overline{p}]^{B-m} = B\,\overline{p}$, this leads to
   $$\sum_{m=0}^{B} m\, P_B(m,\mathbf{b}) = B\left(\prod_{i=1}^{A}\int d\mathbf{s}_i^A\,T_A(\mathbf{s}_i^A)\right)\int d\mathbf{s}^B\,T_B(\mathbf{s}_j^B-\mathbf{b})\,p(\mathbf{s}^B,\{\mathbf{s}_i^A\})\,.$$
2. Consider a cylindrical nucleus of radius R, length $2\,R$ and nuclear density $\rho(\mathbf{b},z) = \frac{1}{2\pi R^3}\,\Theta\,(R-|\mathbf{b}|)\,\Theta\,(2R-z)$. Assume that $R \propto A^{1/3}$, the nuclear number of the cylindrical nucleus A.
   Calculate the nuclear profile function of A and the nuclear overlap function for A+A.
   Determine the average number of participants and the average number of collisions at impact parameter $\mathbf{b}$. How does $\overline{N}_{\rm part}(\mathbf{b})$ and $\overline{N}_{\rm coll}(\mathbf{b})$ scale with A?
   Answer: $T_A(\mathbf{b}) = \frac{1}{\pi R^2}\,\Theta\,(R-|\mathbf{b}|), T_{AA}(\mathbf{b}) = \frac{1}{\left(\pi R^2\right)^2}\,S_{AA}(\mathbf{b})$, where $S_{AA}(\mathbf{b}) \equiv R^2\ (\beta-\sin\beta)$, $\beta \equiv 2\arccos\frac{b}{2R}$. It follows that $\overline{N}_{\rm coll}(\mathbf{b}) = \sigma_{nn}A^2T_{AA}(b) \sim A^{4/3}$ and $\overline{N}_{\rm part}(\mathbf{b}) = 2A\int d\mathbf{s}\,T_A(\mathbf{s})\left[1-\left[1-\sigma_{nn}T_A(\mathbf{s}-\mathbf{b})\right]^A\right] \simeq \frac{2A}{\pi R^2}S_{AA}(\mathbf{b})$ and so $\overline{N}_{\rm part}(\mathbf{b}) \sim A$.

2.2 Characterizing the collisions geometry by multiplicity distributions

Phenomenologically, one finds that soft particle production in nuclear collisions scales approximately with $\overline{N}_{\rm part}^{AB}$ over a wide range of centre-of-mass energy [3]. On the other hand, rare hard processes scale with the number of hard partonic collisions, which is proportional to $\overline{N}_{\rm coll}^{AB}$.

Let us consider a simple model for the average event multiplicity $\overline{n}_{AB}(\mathbf{b})$ in a nucleus–nucleus collision at impact parameter $\mathbf{b}$. We take $\overline{n}_{AB}(\mathbf{b})$ proportional to the mean multiplicity $\overline{n}_{\rm nn}$ of a nucleon–nucleon collision at the same centre-of-mass energy. This is consistent with the assumption that $\overline{n}_{AB}(\mathbf{b})$ arises from the incoherent superposition of an equivalent number of n–n collisions. A model parameter $x \in [0,1]$ allows us to vary the 'equivalent number of n–n collisions' between $\overline{N}_{\rm part}^{AB}(\mathbf{b})$ and $\overline{N}_{\rm coll}^{AB}(\mathbf{b})$,

$$\overline{n}_{AB}(\mathbf{b}) = \left(\frac{1-x}{2}\overline{N}_{\rm part}^{AB}(\mathbf{b}) + x\overline{N}_{\rm coll}^{AB}(\mathbf{b})\right)\overline{n}_{\rm nn}\,. \tag{18}$$

The choice $x=0$, which implies $\overline{N}_{\rm part}^{AB}$-scaling of event multiplicities, is known as the 'wounded nucleon model'. It deserves a special name since total event multiplicities scale approximately proportional to $\overline{N}_{\rm part}^{AB}$ over a wide range of centre-of-mass energy. Varying the model parameter x (within and outside the range favoured by data), we can test the sensitivity of a measurement to details of the mechanism of multi-particle production.

If we had a dynamical model of soft particle production, we could calculate the dispersion d of the mean $\overline{n}_{AB}(\mathbf{b})$. The present set up does not allow us to do so, and the dispersion d is just another model parameter, which we take to be of $O(1)$. This specifies the probability $P(n,\mathbf{b})$ to find a multiplicity n in a particular collision at impact parameter $\mathbf{b}$, if the average event multiplicity is $\overline{n}_{AB}(\mathbf{b})$,

$$P(n,\mathbf{b}) = \frac{1}{\sqrt{2\pi\,d\overline{n}_{AB}(\mathbf{b})}}\exp\left[-\frac{(n-\overline{n}_{AB}(\mathbf{b}))^2}{2\,d\overline{n}_{AB}(\mathbf{b})}\right]\,. \tag{19}$$

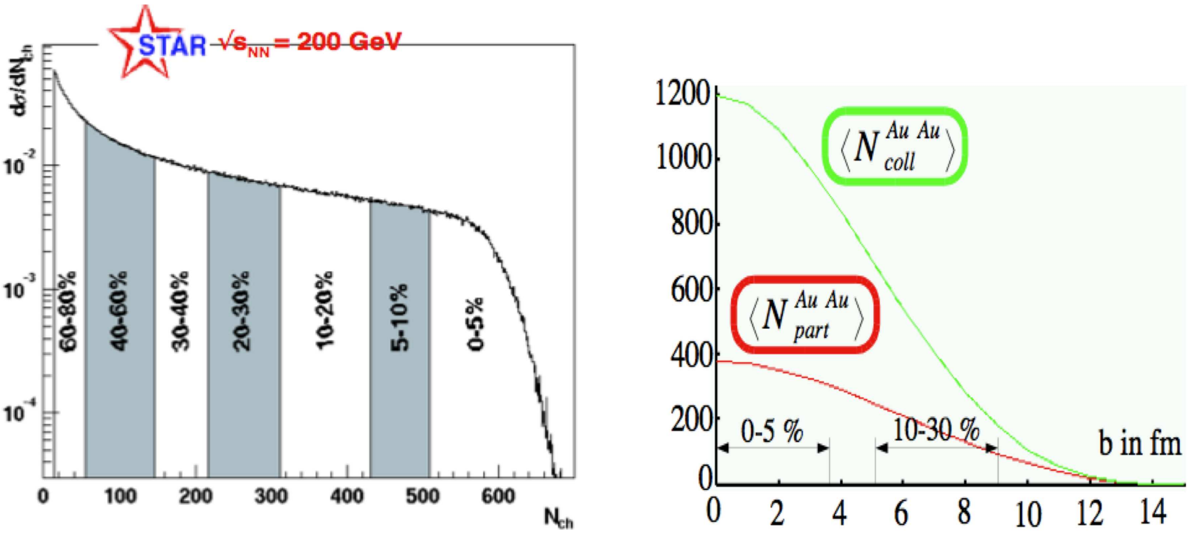

Fig. 2: Left: A typical event multiplicity distribution at RHIC, sliced up in centrality classes. Right: The correlation of the average number of participants and the average number of collisions in a centrality class to the impact parameter in that centrality class. The range of impact parameter, corresponding to 0–5 % and 10–30% centrality is indicated.

The event multiplicity distribution $dN_{\rm ev}/dn$ is obtained by integrating this probability over impact parameter

$$\frac{dN_{\rm ev}}{dn} = \int d\mathbf{b}\, P(n,\mathbf{b}) \left[1 - \left(1 - \sigma_{\rm nn} T_{AB}(\mathbf{b})\right)^{AB}\right] . \qquad (20)$$

Here, the last term in the brackets denotes the probability that an inelastic process occurs, see Equation (13). Equation (20) expresses the event multiplicity distribution as a function of the n–n cross section, the model (18) for the event multiplicity [here defined in terms of $\overline{n}_{AB}(\mathbf{b})$ and its dispersion d], and geometrical information encoded in the nuclear overlap function $T_{AB}(\mathbf{b})$. This information is fully specified by Eq. (17) and the subsequent text.

The curves, plotted in Fig. 1 result from a comparison of (20) with data at RHIC. A more detailed analysis of (20) shows that the shape of $\frac{dN_{\rm ev}}{dn}$ depends largely on the geometrical information encoded in $T_{AB}(\mathbf{b})$, and is rather insensitive to assumptions about the microscopic dynamics underlying soft particle production. This can be checked by varying the parameter x which interpolates between $N_{\rm part}$- and $N_{\rm coll}$-scaling, or varying the dispersion d or even by changing the value of $\sigma_{\rm nn}$. In all these cases, the shape of $\frac{dN_{\rm ev}}{dn}$ changes only mildly, if one adjusts the maximal multiplicity found in the most central collision by a fit parameter. Establishing this observation is left as an exercise.

From the study described above, we conclude that geometrical rather than dynamical information dominates the shape of $\frac{dN_{\rm ev}}{dn}$. As a consequence, the measurement of $\frac{dN_{\rm ev}}{dn}$ is not well-suited to discriminate between different models of multi-particle production, but it is a powerful tool for characterizing centrality classes. The standard procedure is as follows: The distribution $\frac{dN_{\rm ev}}{dn}$ is sliced up in segments, '0–5%' indicating, for example, those five per cent of all collected events which have the highest event multiplicity, see the left-hand side of Fig. 2. These multiplicity classes $n \in [n_0, n_0 + \Delta n]$ are then related to centrality classes, that is to ranges of impact parameter $b \in [b_0, b_0 + \Delta b]$ of the collision. Because of the dispersion of the event distributions in n and b, an event sample at fixed multiplicity will always contain collisions over a finite range of impact parameter. Centrality and multiplicity are correlated, but the accuracy of an event-by-event determination of the impact parameter is limited by the dispersion. To check how accurately the impact parameter can be determined, one can integrate (20) over a finite range of impact parameter, $b \in [b_0, b_0 + \Delta b]$ and compare the resulting event distribution with the corresponding slice on the left-hand side of Fig. 2. This is left as an exercise.

One often characterizes centrality classes by quoting the average number of participants $\langle N_{\rm part}^{AB}\rangle$ in that centrality class,

$$\langle N_{\rm part}^{AB}\rangle_{[n_0,n_0+\Delta n]} = \frac{\int_{n_0}^{n_0+\Delta n} dn\, \int d\mathbf{b}\, P(n,\mathbf{b})\, \left[1-(1-\sigma_{\rm nn}T_{AB}(\mathbf{b}))^{AB}\right]\, N_{\rm part}(\mathbf{b})}{\int_{n_0}^{n_0+\Delta n} dn\, \int d\mathbf{b}\, P(n,\mathbf{b})\, \left[1-(1-\sigma_{\rm nn}T_{AB}(\mathbf{b}))^{AB}\right]}\,. \tag{21}$$

A similar average can be defined for the number of collisions. The correlation between this average and the impact parameter of the collision is shown on the right-hand side of Fig. 2. We note in particular that selecting the 5% most central events in Au–Au collisions amounts to selecting an event sample with an impact parameter up to $|\mathbf{b}| < 3.5$ fm. Since the rate of nucleus–nucleus collisions at impact parameter b is proportional to $b\,db$, there are more collisions at relatively large impact parameter, and the yield of the most central collisions is geometrically suppressed. So, even data from the most central event class contain collisions at significant finite impact parameter.

At the end of this section, it is appropriate to recall the uncertainties and assumptions entering the characterization of centrality classes. Lacking a dynamical model of soft hadron production, we have started from the simple ansatz (18) for the average event multiplicity in a centrality class. Within this framework, we have established that the shape of $\frac{dN_{\rm ev}}{dn}$ is mainly sensitive to the centrality, that is to the impact parameter of the collision, and that it is rather insensitive to details of the model of multiplicity production. We have then tacitly assumed that this holds for all realistic models of multi particle production; then, $\frac{dN_{\rm ev}}{dn}$ is a model-independent tool for the measurement of the impact parameter of the collision. Though this assumption is reasonable, it remains an assumption.

In particular, with increasing centre-of-mass energy, it is conceivable that novel mechanisms of multiparticle production contribute significantly to the event multiplicity. So, even if the relation between multiplicity and centrality of nucleus–nucleus collisions is well-established at some energy scale, cross checks at higher centre-of-mass energies are wanted to put the use of Glauber theory for the centrality determination on a firm footing. One experimental cross-check is to measure the energy E_F of those fragments of a nuclear projectile, which stay at projectile rapidity. These fragments should correspond to those 'spectator' nucleons, which did not participate in the collision, and thus

$$E_F = \left(A - \frac{1}{2}N_{\rm part}(\mathbf{b})\right)\frac{\sqrt{s_{nn}}}{2}\,. \tag{22}$$

This correlation between $N_{\rm part}(\mathbf{b})$, determined experimentally from multiplicity distributions, and E_F is a test of Glauber theory. There are many other tests. At RHIC, for instance, one measured the multiplicity distributions in deuterium–gold (d–Au) collisions under the conditions that i) the proton and neutron in the deuterium both break up, or that ii) the proton interacts with the nucleus while the neutron is detected untouched at forward projectile rapidity. The latter class of p–Au collisions with a spectator neutron selects a more peripheral distribution of impact parameter and comparing the two cases is a sensitive and successful test of Glauber theory (see, for example, Fig. 1 in Ref. [4]).

Questions:

1. Write a short computer program to calculate (20) for the collision of two gold nuclei ($A = 197$).
   Check that the output of this program reproduces the shape of Fig. 1.
   Calculate the integral in (20) restricted to some finite range of impact parameter, (b = 0–4 fm, 4–6 fm, 6–8 fm, etc.) and plot the results. Vary the model parameter x, the value for the dispersion d, the n–n cross section σ_{nn}. To what extent do variations of these parameters affect the centrality classes (b = 0–4 fm, 4–6 fm, 6–8 fm, etc.), which you have calculated before?
2. Use your computer program to calculate (21) and to reproduced the right-hand side of Fig. 2.
3. Our discussion of Glauber theory was limited to the case of a spherical nuclear density $\rho_A(\vec{r}) = \rho_A(r)$.
   There are nuclei which are not spherical but spheroidal, that is with a symmetry axis which is longer than the other two. How would you disentangle an event sample of high centrality, in which this symmetry axis lies parallel to the beam direction, from one in which it is orthogonal to the beam direction? Think about possible confounding factors.
   A detailed discussion can be found in Ref. [5].

2.3 Constraining dynamical models by multiplicity distributions

There are many models of multiparticle production in hadronic collisions, but an understanding from first principles is missing. This is so in proton–proton, as well as in nucleus–nucleus collisions, and resulting uncertainties in the extrapolation to higher centre-of-mass energy are comparable. A compilation of models for the event multiplicity in nucleus–nucleus collisions, and how these models compare to data, can be found in Refs. [6,7]. Here, we do not discuss specific models of multiparticle production. We note, however, that multiparticle production in hadronic collisions shows several characteristic features which persist over many orders of magnitude in $\sqrt{s_{\rm NN}}$, see Ref. [8]. The extrapolation of these apparently generic features to higher centre-of-mass energy shows deviations from the extrapolation of models which have been phenomenologically successful at RHIC [9]. This illustrates that data on the total even multiplicity can help to discriminate between dynamical models of multiparticle production.

We close this section by giving a widely used estimate of the energy density attained in a nucleus–nucleus collision. In the final state of a heavy-ion collision, one can measure the average transverse energy $\langle e_T \rangle$ per produced particle, and the total transverse energy produced in the collision per unit rapidity y, $\frac{dE_T}{dy} \propto \frac{dN_{\rm ev}}{dy} \langle e_T \rangle$. The volume in which this energy was contained at an initial time τ_0, can be obtained by back extrapolating the energy flow along straight lines. For a zero-impact parameter collision between two nuclei of radius R, the total transverse energy is located initially in a transverse area πR^2, and the system has expanded for a short duration τ_0 in the longitudinal 'beam' direction with a speed close to the velocity of light. Bjorken's estimate of the energy density at time τ_0 is given by the transverse energy contained in this initial volume,

$$\epsilon(\tau_0) = \frac{1}{\pi R^2} \frac{1}{\tau_0} \frac{dE_T}{dy} \, . \tag{23}$$

The energy density obtained from Bjorken's estimate is not necessarily equilibrated, it could result equally well from free-streaming particles which do not interact.

3 Particle production with respect to the reaction plane

In the previous section, we have seen how one can select in nucleus–nucleus collisions an event class characterized by a range of finite impact parameter $b \in [b_{\rm min}, b_{\rm max}]$. At finite b, nucleus–nucleus collisions have a reaction plane, which is spanned by the beam axis and the orientation of the impact parameter $\mathbf{b}$ in the transverse plane. In the present section, we shall discuss how to characterize particle production as a function of the azimuthal angle ϕ with respect to the reaction plane.

To get a first idea of why this is interesting, consider the three situations sketched in Fig. 3. A single, jet-like $2 \rightarrow 2$ process would produce the largest azimuthal asymmetry, but such incoherent particle production would not be correlated to the reaction plane. Increasing the event multiplicity by superimposing more incoherent processes, the azimuthal asymmetry will reduce statistically as $\propto 1/\sqrt{n_{\rm ev}}$. Again, this remaining asymmetry is purely statistical; it will point in an arbitrary direction and it will not be correlated to the reaction plane. In contrast, final-state interactions amongst the degrees of freedom produced in the collision are expected to lead to an azimuthal asymmetry which is correlated to the reaction plane. This is so, since the in-medium pathlength of any particle (and thus its probability of interaction) depends on the azimuthal direction ϕ. The correlation of particle production with the reaction plane is interesting, since it gives access to multiparticle final-state interactions and collectivity in the medium.

The picture shown in Fig. 3 is nothing but an illustrative sketch. Whether the $2 - 2$ interactions between particles in the final state is an appropriate picture for understanding nucleus–nucleus collisions, or whether for instance the picture of an evolving fluid is more appropriate, must be established in a data analysis and should not be presupposed by the analysis method employed. The above sketch illustrates, however, that there are in general two sources of azimuthal asymmetries: those caused by statistical fluctuations, which would be present even in the absence of a reaction plane, for instance if the

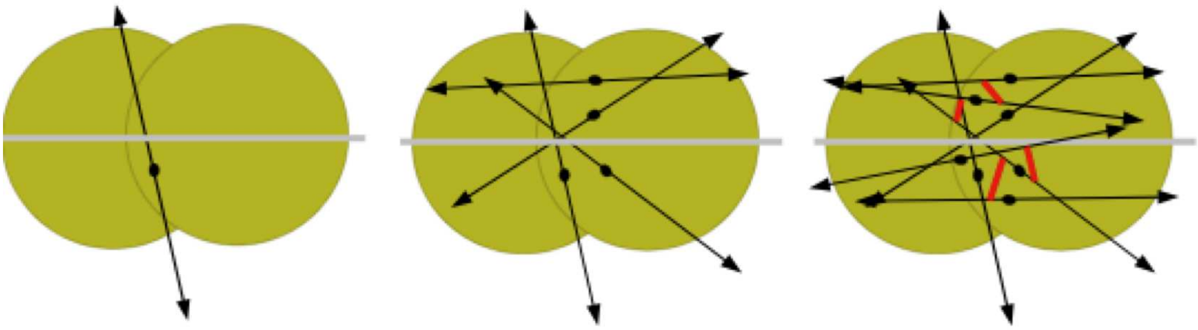

Fig. 3: Sketch of a nucleus–nucleus collision at finite impact parameter. Black dots denote the location of hard processes in the transverse plane. Left and middle: independent 2 → 2 or 2 → n processes lead to an azimuthal asymmetry which decreases with multiplicity and which is not correlated to the reaction plan. Right: final-state interactions have the potential to generate particle correlations with respect to the reaction plane.

heavy-ion collision can be viewed as an incoherent superposition of an equivalent number of nucleon–nucleon collisions. And those which are correlated to the reaction plane and which manifest some form of collective behaviour of the matter produced in the section. In this section, we discuss how to disentangle statistical from collective effects.

We consider a single inclusive particle spectrum $f_1(\mathbf{p}) \equiv \frac{dN}{d^3p}$, where the momentum can be written as $\vec{p} = \left(p_T \cos\phi, p_T \sin\phi, \sqrt{p_T^2 + m^2}\,\sinh y\right)$. The azimuthal asymmetry of this spectrum can be characterized fully in terms of the harmonic coefficients

$$v_n \equiv \langle \exp\left[i\, n\, \phi\right] \rangle = \frac{\int f_1(\mathbf{p})\, e^{i\, n\, \phi}\, d^3p}{\int f_1(\mathbf{p})\, d^3p}\,. \tag{24}$$

The coefficients v_n are called n-th order flow. In general, they can depend on the transverse momentum p_T, the rapidity y, and they can differ for different particle species. In particular, v_1 is referred to as 'directed flow' and v_2 as elliptic flow. In the collision of identical nuclei at mid-rapidity, the collision region is symmetric under $\phi \to -\phi$ and all odd harmonics vanish. In this case, the elliptic flow v_2 is the first non-vanishing coefficient.

3.1 The cumulant method for n-th order flow

The coefficients (24) cannot be measured directly, since the orientation of the reaction plane is not known a priori. The cumulant method is a systematic approach for relating v_n to measurable quantities, which has been pioneered by [10]. It is based on the analysis of particle correlations. We consider a two-particle inclusive distribution $f(\mathbf{p}_1, \mathbf{p}_2)$ and we perform the harmonic transformation

$$\langle f(\mathbf{p}_1, \mathbf{p}_2) \rangle \equiv \langle \exp\left[i\, n\, (\phi_1 - \phi_2)\right] \rangle = \frac{\int \exp\left[i\, n\, (\phi_1 - \phi_2)\right]\, f(\mathbf{p}_1, \mathbf{p}_2)\, d^3p_1\, d^3p_2}{\int \langle\, f(\mathbf{p}_1, \mathbf{p}_2)\, d^3p_1\, d^3p_2}\,. \tag{25}$$

Measuring this particle correlation does not require a priori knowledge about the orientation of the reaction plane and it is thus measurable. In general, a two-particle distribution has an uncorrelated part, and a correlated one,

$$f(\mathbf{p}_1, \mathbf{p}_2) = f(\mathbf{p}_1)\, f(\mathbf{p}_2) + f_c(\mathbf{p}_1, \mathbf{p}_2)\,. \tag{26}$$

The key idea of the cumulant method is to count the correlated part f_c as suppressed by one factor $\sim 1/n_{\text{ev}}$ of the event multiplicity, compared to the leading contribution. For instance, consider the simplified case that $n_{\text{ev}} = 2N$ particles are produced in $2 - 2$ processes, so that any particle is dynamically correlated with exactly one other particle, namely its recoil, and it is uncorrelated with the $2N - 1$ other particles (see Fig. 3). In this case, the correlated part is $O(1/n_{\rm ev})$-suppressed. An analogous argument holds for other dynamical correlations between particle pairs, for instance dynamical correlations due to resonance decays. Consider $n_{\rm ev}$ pions, some of them stemming from ρ-decays: each pion will have exactly one resonance decay partner with which it is correlated, and (as long as there is no collective effect which correlates the motion of particles to the global event) it will be uncorrelated with $(n_{\rm ev} - 1)$ pions. In short, on the right-hand side of Eq. (26), the first term retains the information about collectivity, from which the harmonic coefficients v_n in (24) can be calculated. The second term separates two-particle correlations which are typically due to resonance decays or conservation laws and which would fake azimuthal asymmetries not correlated to the reaction plane. Having separated the correlated part in (26), we can write the average (25) as

$$\langle \exp\left[i\, n\, (\phi_1 - \phi_2)\right]\rangle = v_n\, v_n + \underbrace{\langle \exp\left[i\, n\, (\phi_1 - \phi_2)\right]\rangle_c}_{O(1/n_{\rm ev})} \,. \tag{27}$$

The correlated part, which is suppressed by $O(1/n_{\rm ev})$, is often referred to as non-flow correction. It is possible to measure from two-particle correlations (27) the azimuthal asymmetry v_n of a single inclusive hadron spectrum with respect to the reaction plane, if the signal v_n^2 is larger than the non-flow correction, that means

$$v_n \gg 1/\sqrt{n_{\rm ev}} \qquad \text{for two-particle correlations.} \tag{28}$$

What if this condition is not satisfied? One can enhance the sensitivity of the construction by going to the 4th order cumulant

$$\begin{aligned} \langle\langle \exp\left[i\, n\, (\phi_1 + \phi_2 - \phi_3 - \phi_4)\right]\rangle\rangle \;\equiv\; & \langle \exp\left[i\, n\, (\phi_1 + \phi_2 - \phi_3 - \phi_4)\right]\rangle \\ & - \langle \exp\left[i\, n\, (\phi_1 - \phi_4)\right]\rangle \langle \exp\left[i\, n\, (\phi_2 - \phi_4)\right]\rangle \\ & - \langle \exp\left[i\, n\, (\phi_1 - \phi_4)\right]\rangle \langle \exp\left[i\, n\, (\phi_2 - \phi_3)\right]\rangle \,. \end{aligned} \tag{29}$$

Here, the subtraction terms are chosen such that the leading non-flow corrections cancel. Upon explicit calculation, one finds

$$\langle\langle \exp\left[i\, n\, (\phi_1 + \phi_2 - \phi_3 - \phi_4)\right]\rangle\rangle = -v_n^4 + O\left(\frac{1}{n_{\rm ev}^3}\right) + O\left(\frac{v_{2n}^2}{n_{\rm ev}^2}\right) \,. \tag{30}$$

In practice, the higher harmonics v_{2n} are much smaller than v_n. Then, to determine the azimuthal asymmetry v_n from (30), we require that the signal

$$v_n \gg 1/{n_{\rm ev}}^{3/4} \qquad \text{for two-particle correlations.} \tag{31}$$

So, by going to a higher cumulant, we have eliminated 4-particle correlations, which would fake a correlation with the reaction plane in a second-order cumulant analysis, and we have enhanced the sensitivity for discriminating the signal (24) from confounding correlations. One can show that by going to even higher cumulants, one can achieve asymptotically a sensitivity $v_n \gg 1/n_{\rm ev}$.

3.2 Elliptic flow at RHIC

On the left-hand side of Fig. 4, we show the transverse momentum dependence of the elliptic flow v_2, measured for different centrality classes in Au-Au collisions at RHIC. The azimuthal asymmetry v_2 of the final-state single inclusive hadron spectrum is maximal in semi-peripheral collisions. v_2 decreases for more peripheral centrality classes. This is so since v_2 measures a collective phenomenon originating from final-state interactions, and the latter become less important with increasing impact parameter and smaller system size. On the other hand, v_2 decreases towards more central collisions, since the initial geometric asymmetry is decreased. However, while v_2 is constructed such that it should disappear for the idealized case of an event sample at impact parameter $b = 0$, v_2 does not disappear in the sample of the

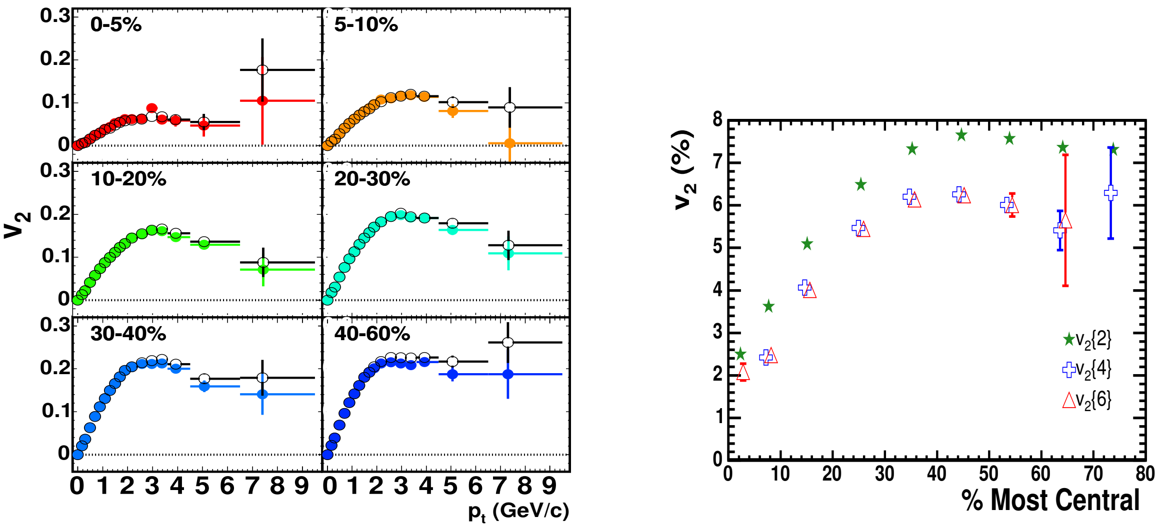

Fig. 4: Left: Transverse momentum dependence of the elliptic flow v_2 for different centrality bins. Right: the p_T-integrated elliptic flow v_2 as a function of centrality bins, reconstructed with 2nd, 4th and 6th order cumulants. The most central bin is to the left. Figures taken from Ref. [11].

5% most central collisions. This is so, since even the most central 5% of the total nucleus–nucleus cross section is an event sample with sizeable average impact parameter, see our discussion in Section 2.2.

To appreciate the total size of the v_2 signal, we note that the harmonic coefficients v_n characterize deviations of the single inclusive spectra from azimuthal symmetry as

$$\frac{\mathrm{d}N}{\mathrm{d}^2\mathbf{p}_t\,\mathrm{d}y} = \frac{1}{2\pi}\frac{\mathrm{d}N}{p_T\,\mathrm{d}p_T\,\mathrm{d}y}\left[1 + 2v_1\cos(\phi-\Phi_R) + 2v_2\cos 2(\phi-\Phi_R) + \cdots\right], \tag{32}$$

where Φ_R denotes the azimuth (in the laboratory frame) of the reaction plane. In particular, the $\cos 2\phi$ term has the prefactor $2\,v_2$. So, if v_2 reaches a value of $v_2 \sim 0.2$, then the term in brackets in (32) varies between 0.6 and 1.4. This implies that there are more than twice as many particles emitted in the reaction plane than orthogonal to it. In short, the measured azimuthal asymmetry is large.

We now discuss whether the experimentally measured signal $v_2 \sim 0.2$ is caused by random fluctuations not correlated to the reaction plane, or whether it is indicative of a collective phenomenon. For a simple estimate, we consider the typical case that the events for which v_2 is determined have of the order of $n_{\mathrm{ev}} \sim 100$ final-state particles in the phase space region which is analysed. Assume that we determine v_2 form 2nd order cumulants. For the result to be dominated by collective effects, we require according to (28) that $v_n \gg 1/\sqrt{n_{\mathrm{ev}}} \sim 0.1$. For $v_n \sim 0.2$, this condition is not realized. So, we expect that the result of a 2nd order cumulant analysis of v_2 contains non-negligible non-flow effects. What about a 4th order cumulant analysis? The signal $v_2 \sim 0.2$ is indeed much larger than $1/n_{\mathrm{ev}}^{3/4} \sim 0.03$, so the inequality (31) holds. As a consequence, we expect that the result of a 4th order cumulant analysis is stable and that no further non-flow corrections are found if even higher order cumulants are included in the analysis. This is confirmed in the data analysis, see Fig. 4. In short, by disentangling effects from random fluctuations from collective ones, we have established a signal v_2 which is large and which can be attributed to a collective phenomenon.

4 Hydrodynamic modelling of heavy-ion collisions

In the previous section, we have established for the azimuthal asymmetry v_2 a benchmark in which collective effects are absent and where the signal is due to random fluctuations only. We have then established that the measured value of v_2 is significantly larger than this benchmark, we have disentangled the effect of random fluctuations from the signal of a collective phenomenon by a cumulant analysis, and we have arrived at a value for v_2 which can be attributed to a collective phenomenon.

The question arises to what extent the dynamical origin of this collective phenomenon can be constrained in an interplay of theory and data analysis. What we know is that in nucleus–nucleus collisions at finite impact parameter, the nuclear overlap region of the collision covers initially an almond-shaped, azimuthally asymmetric region in the transverse plane. Upon impact, the distribution of the produced particles is asymmetric in transverse space, but initially it is symmetric in transverse momentum space. So, the value of v_2 must arise from a mechanism that translates the initial *geometrical* anisotropy into a final-state *momentum-space* anisotropy. This mechanism will be the more efficient the more the produced degrees of freedom interact with each other after being produced. The maximal signal v_2 may be expected to arise from a hydrodynamical picture of the collision, since any dissipative effect (indicative, for example, of a finite mean-free path between interactions) is expected to reduce v_2.

So, the first motivation for a modelling of heavy-ion collisions in terms of a fluid is the idea to start from a description which conceivably explores the case of a maximal degree of collectivity. Here we discuss the basis for such model simulations, and how they compare to data on v_2.

4.1 Tensor decomposion of $T^{\mu\nu}$

We consider matter in local equilibrium, characterized by its energy momentum tensor $T^{\mu\nu}(x)$ and n charge densities $N_i^\mu(x)$, $i \in [1, n]$. In much of what follows, we do not spell out explicitly the dependence of these thermodynamic fields on the space-time coordinate x. The energy momentum tensor is symmetric under exchange of Lorentz indices, so we have

$$\text{energy momentum tensor} \quad T^{\mu\nu} \qquad \ldots 10 \,\text{indep. functions} \tag{33}$$

$$\text{conserved charges} \quad N_i^\mu \qquad \ldots 4n \,\text{indep. functions} \tag{34}$$

We introduce now a local flow field $u_\mu(x)$, defined by a normalized vector $u_\mu\, u^\mu = 1$. The projector on the subspace orthogonal to the flow field is

$$\Delta_{\mu\nu} = g_{\mu\nu} - u_\mu u_\nu \,. \tag{35}$$

In a tensor decomposition with respect to the flow field, one can disentangle properties which are comoving with the local flow field from those which are leaking out of the comoving rest frame. For the energy momentum tensor, this tensor decomposition reads

$$T^{\mu\nu} = \epsilon\, u^\mu\, u^\nu - p\, \Delta^{\mu\nu} + q^\mu u^\nu + + q^\nu u^\mu + \Pi^{\mu\nu} \,. \tag{36}$$

Here, the different components of $T^{\mu\nu}$ have specific physical interpretations. For instance, the projection

$$\epsilon = u_\mu\, T^{\mu\nu}\, u_\nu \tag{37}$$

defines the energy density comoving with the flow field. This can be seen clearly, for instance, by observing that in the frame locally comoving with the fluid, $u_\mu = (1, 0, 0, 0)$, the energy density ϵ is the 00-component of the energy-momentum tensor. Similarly, the isotropic pressure is given by

$$p = -T^{\mu\nu}\, \Delta_{\mu\nu}/3 \,, \tag{38}$$

which in the locally comoving frame with $u_\mu = (1, 0, 0, 0)$ reduces to the spatial diagonal ii-component of $T^{\mu\nu}$. The heat flow

$$q^\mu = \Delta^{\mu\alpha} T_{\alpha\beta}\, u^\beta \tag{39}$$

characterizes the energy density which dissipates out of the rest frame locally comoving with the fluid velocity u_μ. The last term of the tensor decomposition (36) is the traceless shear viscous tensor

$$\Pi^{\mu\nu} = \left[\left(\Delta^\mu_\alpha \Delta^\nu_\beta + \Delta^\mu_\beta \Delta^\nu_\alpha \right) /2 - \Delta^{\mu\nu} \Delta_{\alpha\beta}/3 \right] T^{\alpha\beta} \,. \tag{40}$$

The so-called Landau frame is characterized as the frame comoving with the physical 4-velocity of the energy flow. The Landau flow velocity satisfies the implicit equation

$$u_L^\mu \equiv \frac{T^\mu_\nu\, u_L^\nu}{\sqrt{u_L^\alpha\, T^\beta_\alpha\, T_{\beta\gamma}\, u_L^\gamma}}\,. \tag{41}$$

In the Landau frame, the heat flow vanishes by construction,

$$q^\mu = 0 \qquad \text{in Landau frame.} \tag{42}$$

In the absence of conserved charges, or if one restricts the discussion to cases for which the flow of conserved charges does not differ from the flow of energy, the Landau frame is a natural choice, since it defines the local rest frame of the fluid.

For the conserved charge current $N^\mu(x)$, the corresponding tensor decomposition takes the form

$$N_i^\mu = n_i\, u^\mu + \overline{n}_i^\mu\,. \tag{43}$$

Here, n_i is the charge density locally comoving with the flow field.

$$\overline{n}_i^\mu = \Delta^\mu_\nu\, N_i^\nu \tag{44}$$

is orthogonal to the flow field and characterizes the charge dissipating out of the locally comoving fluid element. For each charge, we can specify the local rest frame comoving with the net charge, characterized by the flow velocity

$$u_E^\mu \equiv \frac{N_i^\mu}{\sqrt{N_i^\mu N_{i\mu}}}\,. \tag{45}$$

In this so-called Eckard frame, net charge does not flow out of the local rest frame, so $\overline{n}_i^\mu = 0$ by construction. This amounts to replacing the three independent functions $\overline{n}_i^\mu(x)$ by the three independent functions of the Eckard velocity u_E^μ. In what follows, we shall work mainly in the Landau frame.

4.2 Equations of motion for a perfect fluid

A fluid is called perfect if we can associate to each space-time point x a fluid velocity, such that in the frame comoving with this velocity, the fluid is isotropic at x. So, for each x, there is a fluid rest frame such that $T^{00}(x) = \epsilon(x)$, $T^{ij}(x) = p(x)\,\delta^{ij}$ and $N_i^\mu(x) = n_i(x)\delta^{\mu 0}$. It follows that in a frame specified by an arbitrary velocity $u_\mu(x)$, the charge currents and energy-momentum tensor of a perfect fluid take the form

$$\begin{aligned} N_i^\mu &= n_i\, u_\mu\,, && (46)\\ T^{\mu\nu} &= \epsilon\, u^\mu\, u^\nu - p\,\Delta_{\mu\nu}\,. && (47)\end{aligned}$$

This is a tremendous simplification of the general case. The $10+4n$ independent functions entering (33) and (34) are reduced to $5+n$ unknown functions, namely ϵ, p, three independent functions $u^\mu(x)$ and the n functions $n_i(x)$. The conservation laws for the conserved charges and energy-momentum give $4+n$ constraints, namely n constraints for the conserved charges and 4 constraints for the energy momentum tensor,

$$\begin{aligned} \partial_\mu\, N_i^\mu &= 0\,, && (48)\\ \partial_\mu T^{\mu\nu} &= 0\,. && (49)\end{aligned}$$

To fully determine the equations of motion for the $5+n$ unknowns of in (46), (47), we need one additional constraint. This is provided by the equation of state (e.o.s.), which expresses the pressure p in terms of the energy density and charge densities,

$$p = p(\epsilon, n)\,. \tag{50}$$

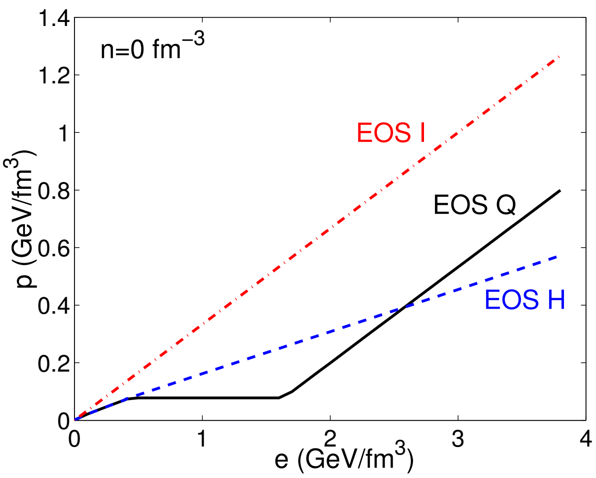

Fig. 5: Three model equations of state of QCD matter: a hard e.o.s. (EOS I), a soft e.o.s. (EOS H), and an e.o.s. which displays a 1st order phase transition from a soft 'hadronic' e.o.s. at low density to a 'hard' partonic e.o.s. at high density. Figure taken from [12].

For a perfect fluid, information about the underlying theory enters only by specifying the equation of state (50). A main characteristic of the equation of state is the velocity of sound

$$c_s^2 = \frac{\partial p}{\partial \epsilon}\,. \tag{51}$$

An ideal gas has $c_s^2 = 1/3$ and equations of state which come close to this velocity of sound are referred to as 'hard'. In a hadron gas, an increase of energy density does not translate as efficiently into a change of pressure, since it leads also to the excitation of higher lying resonances. As a consequence, a hadron gas is expected to have a much softer equation of state with $c_s^2 \approx 0.15$. Figure 5 shows a set of different equations of state, used in fluid model simulations of heavy-ion collisions. Realistic model equations of state extrapolate between a soft 'hadronic' regime at low density and a hard 'partonic' regime at high density.

4.3 Bjorken boost-invariant ideal fluid

A fluid is called Bjorken boost-invariant, if the longitudinal velocity v_z of the frames locally comoving with the fluid is related to their space-time position like $v_z = z/t$. Here as always, the 'longitudinal' coordinate z refers to the direction parallel to the beam. The condition of longitudinal boost-invariance takes a particularly simple form in terms of proper time τ and space-time rapidity η,

$$t = \tau \cosh\eta\,, \tag{52}$$

$$z = \tau \sinh\eta\,. \tag{53}$$

Now,

$$v_z = \frac{z}{t} = \tanh\eta\,, \qquad \text{for Bjorken boost-invariant velocity profile.} \tag{54}$$

A fluid with this velocity distribution will look the same in all longitudinally comoving fluid elements. This distribution is of particular interest in the modelling of heavy-ion collisions, since one expects that at high centre-of-mass energy, the initial conditions of the fluid produced satisfy (54) over a wide range of rapidity. Moreover, one can show that if (54) is satisfied by the initial conditions, then it is preserved by the equation of motion (49). This implies that the longitudinal dynamics is trivial and decouples: one is left with a set of 2+1-dimensional hydrodynamic equations of motion in the transverse plane, which are computationally less demanding.

To illustrate the consequences of Bjorken boost-invariant flow, we consider here a one-dimensional toy model with equations of motion

$$\begin{aligned} \partial_t T^{00} + \partial_z T^{z0} &= 0\,, && (55)\\ \partial_t T^{0z} + \partial_z T^{zz} &= 0\,. && (56)\end{aligned}$$

Assuming that the energy-momentum tensor is of the ideal form (47), and going to the coordinates (52), (53), we find

$$\begin{aligned} \frac{p+\epsilon}{\tau}\cosh\eta + \frac{\sinh\eta}{\tau}\frac{\partial p}{\partial\eta} + \frac{\partial\epsilon}{\partial\tau}\cosh\eta &= 0\,, && (57)\\ \frac{p+\epsilon}{\tau}\sinh\eta + \frac{\cosh\eta}{\tau}\frac{\partial p}{\partial\eta} + \frac{\partial\epsilon}{\partial\tau}\cosh\eta &= 0\,. && (58)\end{aligned}$$

Combining these equations leads to

$$\begin{aligned} \left.\frac{p+\epsilon}{\tau} + \frac{\partial\epsilon}{\partial\tau}\right|_\eta &= 0\,, && (59)\\ \left.\frac{\partial p}{\partial\eta}\right|_\tau &= 0\,. && (60)\end{aligned}$$

The equations of motion in η and τ decouple. There is no pressure gradient in η, and this implies that the initial velocity $v_z = z/t$ remains unchanged throughout the dynamical evolution. The new coordinates (η, τ) already take the scaling expansion into account.

The fundamental thermodynamic relation $\epsilon + p = \mu_i n + T\,s$ allows us to relate energy density and pressure to the temperature T, the entropy density s and the chemical potentials μ and charge densities n of the system. In the absence of conserved charges, we have

$$\epsilon + p = T\,s\,. \qquad (61)$$

The equation of motion (59) can now be rewritten as an evolution equation for the entropy density,

$$\left.\frac{s}{\tau} + \frac{\partial s}{\partial\tau}\right|_\eta = 0\,. \qquad (62)$$

The solution of this differential equation is

$$s = \frac{\text{const.}}{\tau} \qquad \text{at constant } \eta\,. \qquad (63)$$

Since the one-dimensional volume of the system expands proportional to τ, the total entropy is $S = s\,\tau = \text{const}$. This is so not only for this toy model but in general: as long as thermodynamic fields do not develop discontinuities, a perfect fluid is a system with isentropic expansion. That means, entropy is not produced during the evolution.

Similarly, we can explore the temperature dependence of the energy density. Writing $dp = c_s^2\, d\epsilon = s\,dT = \frac{\epsilon+p}{T} dT = \left(1 + c_s^2\right)\epsilon\,\frac{dT}{T}$, we find

$$\frac{d\epsilon}{\epsilon} = \frac{1+c_s^2}{c_s^2}\,\frac{dT}{T} \qquad \longrightarrow \qquad \epsilon \propto T^{1+c_s^{-2}}\,. \qquad (64)$$

For the case of the equation of state of an ideal gas, $\epsilon = 3\,p$, these expressions reduce to some widely known parametric dependence. The solution of (59) is now $\epsilon \propto \tau^{-4/3}$, the temperature decreases for the

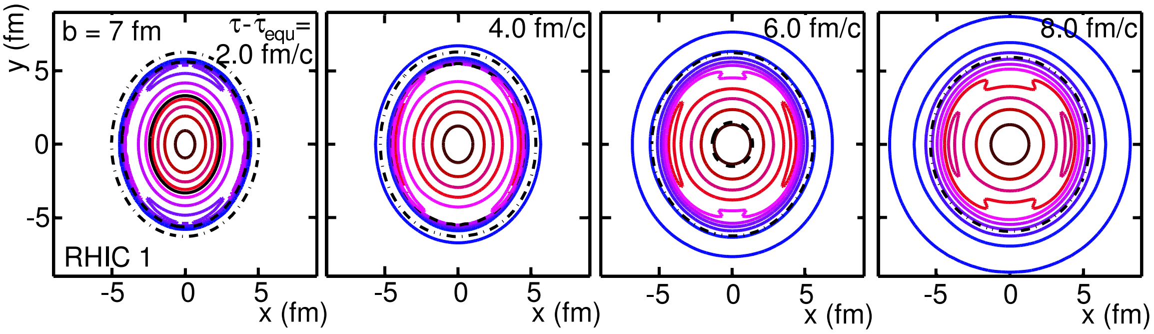

Fig. 6: Results of a fluid dynamic simulation of a Au+Au collision at impact parameter $b = 7$ fm. The plots show contours of constant energy density in the transverse plane at different times 2, 4, 6 and 8 fm/c after initialization of the simulation. Figure taken from Ref. [13].

case of one-dimensional Bjorken expansion like $T \propto \tau^{-1/3}$, and the energy density (64) is proportional to the 4th power of the temperature.

Despite its simplicity, the features of this 1+1-dimensional model provide some useful insights into the physics of 3+1-dimensional fluid simulations. To understand why this is so, consider a small patch in the transverse plane of a heavy-ion collision which has a boost-invariant velocity profile. As long as the hydrodynamic distributions in the vicinity of this patch show negligible gradients in the transverse direction, the hydrodynamical evolution in the transverse plane is negligible and the main characteristics of the time evolution are captured by the 1+1-dimensional model mentioned above.

4.4 Simulating a Bjorken boost-invariant perfect fluid

In this section, we discuss fluid dynamic simulations of heavy-ion collisions. We restrict the discussion to the widely studied case of a Bjorken boost-invariant perfect fluid. In this case, the longitudinal dynamics (60) decouples, one is left with a 2+1 dimensional problem. While the fluid dynamic equations of motion do not require model-dependent assumptions, such assumptions enter the initial conditions, the choice of the equation of state and the interfacing of the fluid dynamic simulation with the hadronic final state. We now comment on these aspects in more detail:

For a heavy-ion collision at impact parameter b, the initial transverse geometry is determined by the nuclear overlap function, see Section 2. Realistic choices of the transverse r-dependence of thermodynamic fields typically base a model ansatz for the energy density or entropy distribution on this geometrical information. For instance, since entropy is conserved under perfect fluid dynamic evolution, it is expected to scale with the final-state multiplicity. This can serve as a motivation for invoking the Glauber model and writing the entropy density distribution in the transverse coordinate $\mathbf{r}$ as a function of the number of participants $N_{\rm part}(\mathbf{b}, \mathbf{r})$ or the number of collisions $N_{\rm coll}(\mathbf{b}, \mathbf{r})$, which for a collision at impact parameter $\mathbf{b}$ occur at transverse position $\mathbf{r}$. A typical ansatz, with the interpolating model parameter x introduced in (18) is

$$s_{\rm init}(\mathbf{r}) = s(\tau_0, \mathbf{r}, \eta = 0) \propto \left(\frac{1-x}{2} \overline{N}^{AB}_{\rm part}(\mathbf{b}, \mathbf{r}) + x \overline{N}^{AB}_{\rm coll}(\mathbf{b}, \mathbf{r}) \right) . \qquad (65)$$

The normalization of this transverse entropy density distribution at initial time τ_0 is fixed by the final-state multiplicity which determines the total entropy in the final state. The energy density is obtained from this expression by use of the equation of state and the fundamental thermodynamic relation (61). Alternatively, one sometimes starts from an ansatz of the energy density which satisfies the same functional form as (65). In short: there are some uncertainties in specifying the initial energy density distribution, but they are constrained by information about the initial transverse geometry of the collision.

Aside from the initial energy density, a perfect fluid dynamic simulation requires specification of the initial transverse flow field. Since there is no a priori reason why transverse position and momentum should be correlated at initial time τ_0, the standard assumption is that the transverse flow will arise solely within the fluid dynamic evolution along the spatial density gradients, so that initially $u_\mu(\tau_0) = (1, 0, 0, 0)$ in the entire transverse plane. Figure 6 may illustrate how a non-vanishing transverse flow field builds up during the simulation. A finite impact parameter collision leads initially to an almost elliptic *geometrical* anisotropy of the energy density distribution in the transverse plane. This implies that density gradients are larger in the reaction plane (the x-direction in Fig. 6) then orthogonal to it. A stronger density gradient induces a larger increase in flow. As a result, the system is seen to evolve faster within the reaction plane then orthogonal to it. The dynamical evolution translates an initial geometric asymmetry into a final-state momentum asymmetry. (Information about the latter is not given directly in Fig. 6, but it is shown in Fig. 7 below. It may also be deduced from the above narrative of the time sequence shown.)

A perfect fluid dynamical simulation, initialized as mentioned above, describes the expansion of the high-density fluid within the transverse plane. Within a hydrodynamical framework, this evolution can be continued to arbitrarily late times and thus to arbitrarily low densities. However, on physical grounds one expects that below a critical energy density ϵ_c, the microscopic reaction rates in the system are not large enough to maintain local equilibrium. At this stage of the evolution, a fluid dynamic description starts to break down and must be interfaced with another dynamic description. The simplest interface is the so-called sharp Cooper–Frye freeze-out condition. It assumes that if the energy density at the space-time point x reaches the critical value $\epsilon(x) = \epsilon_c$, then this fluid element 'freezes out'. This freeze-out condition is realized on a three-dimensional hypersurface $\Sigma(x)$ in 4-dimensional space. The Cooper–Frye freeze-out condition translates the energy density on $\Sigma(x)$ into a corresponding yield of free-streaming hadrons

$$E\frac{dN_i}{d\vec{p}} = \frac{g_i}{(2\pi)^3} \int_\Sigma \vec{p}.d\vec{\sigma}(x)\, f_i(p.u(x), x)\,. \tag{66}$$

The different hadron species i are distributed statistically according to a thermal distribution,

$$f_i(E, x) = \frac{1}{\exp\left[\left(E - \mu_i(x)\right)/T(x)\right] \pm 1}\,. \tag{67}$$

Here, the local temperature $T(x)$ is the freeze-out temperature on $\Sigma(x)$, and the μ_i are local chemical potentials, relevant for hadrons which carry conserved charges such as baryon number or strangeness. In the single inclusive hadron spectrum (66), these distributions appear boosted with local flow velocity $u_\mu(x)$ at freeze-out. In this way, all hadron species emerge from the same underlying flow field.

In principle, one expects that between a hydrodynamic evolution of a sufficiently dense system, and the free-streaming of particles, there should be a collision phase in which particles have finite mean free path and scatter repeatedly. To what extent such a hadronic rescattering phase cannot be mimicked by interfacing perfect fluid dynamics with a sharp freeze-out condition is a matter of ongoing debate, which we do not address here. Rather, we close this section by showing in Fig. 7 some comparisons of RHIC data with a fluid dynamic simulation, supplemented by sharp Cooper–Frye freeze-out. The magnitude of the p_T-integrated elliptic flow is well-reproduced in these collisions for sufficiently large system size, i.e., for sufficiently high centrality. For peripheral collisions, however, the azimuthal asymmetry of a fluid dynamic evolution exceeds that in the data. This is often argued to be an indication that the system becomes too small to be describable as a perfect fluid. On the other hand, fluid dynamics reproduces the hadron species dependence of the p_T-differential azimuthal symmetry rather well up to $p_T \lesssim 2$ GeV. This gives strong support to a hydrodynamic picture since the hadron species dependence arises without additional fit parameter as the consequence of emitting hadrons of different masses from the same collective flow field. At high transverse momentum [Fig. 7(b)], one sees again deviations of the fluid dynamic simulations from data, but these one may have expected since high-p_T hadrons are likely not fully equilibrated.

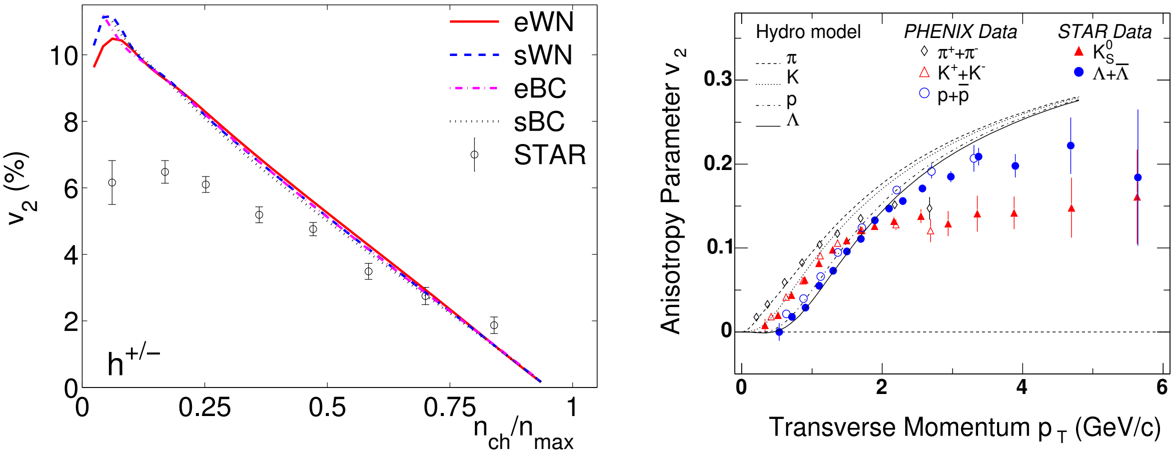

Fig. 7: Left: Transverse momentum averaged elliptic flow for $\sqrt{s_{\rm NN}} = 130$ GeV Au+Au collisions as a function of collision centrality ($n_{\rm ch}$ is the charged multiplicity at mid-rapidity). The curves are results of fluid dynamical simulations with different choices for the initial energy density profile. Right: The elliptic flow $v_2(p_T)$ as a function of transverse momentum for identified hadrons from minimum bias Au+Au collisions at $\sqrt{s_{\rm NN}} = 200$ GeV, together with curves from fluid dynamical simulations. Figure taken from Ref. [14].

4.5 Dissipative corrections to perfect fluid dynamics

So far, we have discussed hydrodynamic simulations under the assumption that the fluid is perfect. When is this assumption valid? To identify the relevant quantities for addressing this question, let us consider first a conserved current $j^\mu = \rho\, u^\mu$. Current conservation leads to

$$\partial_\mu\, j^\mu = \rho\, \partial_\mu u^\mu + u^\mu \partial_\mu \rho = 0\,. \tag{68}$$

Here, $u^\mu \partial_\mu$ is the comoving time derivative, which becomes ∂_t in the rest frame comoving with the fluid velocity. The second combination of partial derivative and velocity field is the expansion scalar

$$\Theta \equiv \partial_\mu u^\mu\,, \tag{69}$$

which measures locally a spatio-temporal variation of the macroscopic fluid, namely its velocity gradient. Physically, equilibrium (and thus isotropy) is maintained locally in a fluid due to microscopic reactions. If the velocity gradients in the system are too large, then these reaction rate Γ_{rr} cannot catch up any more, dissipative processes become relevant and local isotropy is lost. So, a perfect fluid assumption is valid if

$$\Gamma_{\rm reaction\,rate} \gg \Theta = \partial_\mu u^\mu\,, \qquad \text{for a perfect fluid.} \tag{70}$$

These considerations convey the general idea that dissipative corrections to a perfect fluid can be characterized in a gradient expansion.

If more than the 5 independent functions of the perfect form (46) of the energy momentum tensor are relevant, then the constraints of energy–momentum conservation (49) and equation of state (50) are not sufficient to close the set of equations of motion. To obtain additional constraints, one standard procedure is to invoke the 2nd law of thermodynamics. For a perfect fluid, the entropy flow is $S^\mu = s\, u^\mu$. We now consider a gradient expansion of S^μ to first order, that is we look for the most general ansatz of the entropy flow. In the Eckart frame, we have to first order the dissipative quantities q^μ, $\Pi^{\mu\nu}$ and $\Pi = p_{\rm eq} - p$ which denotes the difference between the expected local pressure in case of local equilibrium (defined as $p_{\rm eq} = p(\epsilon, n)$) and the measured local pressure p which can now deviate from equilibrium. The most general ansatz is

$$S^\mu = s\, u^\mu + \beta\, q^\mu\,, \tag{71}$$

where β is an as yet unknown multiplier. For this ansatz, one can show

$$T\,\partial_\mu S^\mu = (T\beta - 1)\,\partial.q + q.\,(\dot{u} + T\partial\beta) + \Pi^{\mu\nu}\partial_\nu\, u_\mu + \Pi\,\Theta \geq 0\,. \tag{72}$$

It follows from the 2nd law of thermodynamics that the right-hand side of this equation must be positive for all space-time points. To satisfy this condition, one chooses

$$\begin{aligned} \beta &= 1/T\,, &(73)\\ \Pi &= \zeta\,\Theta\,, &(74)\\ q^\mu &= \kappa\,T\,\Delta^{\mu\nu}\left(\partial_\nu \ln T - \dot{u}_\nu\right)\,, &(75)\\ \Pi^{\mu\nu} &= 2\eta_{\mathrm{shear}}\left[\frac{1}{2}\left(\Delta^\mu_\alpha\Delta^\nu_\beta + \Delta^\nu_\alpha\Delta^\mu_\beta\right) - \frac{1}{3}\Delta^{\mu\nu}\Delta_{\alpha\beta}\right]\partial^\alpha u^\beta\,. &(76) \end{aligned}$$

Here, we have introduced the bulk viscosity ζ, the thermal conductivity κ and the shear viscosity η_{shear}. With these definitions, Eq. (72) becomes

$$\partial_\mu S^\mu = \frac{\Pi^2}{\zeta T} - \frac{q.q}{\kappa T^2}\frac{\Pi^{\mu\nu}\Pi_{\mu\nu}}{2\eta_{\mathrm{shear}}T} \geq 0\,. \tag{77}$$

So, by construction entropy does not decrease at any space-time point. The definitions (73)–(76) provide a set of constraints which ensure the 2nd law of thermodynamics. They define the a priori independent functions Π, $\Pi^{\mu\nu}$ and q^μ of the energy momentum tensor in terms of velocity gradients, and they thus close the system of equations of motion. This framework is referred to as relativistic Navier–Stokes hydrodynamics or 1st order dissipative fluid dynamics, as it includes gradients only up to first order.

A non-vanishing bulk viscosity can arise if internal degree of freedom are excited in a fluid. In such a case, an increase in energy density is not accompanied instantaneously by the corresponding increase in pressure, but goes for instance into higher excited resonances. In the partonic phase of QCD, such mechanisms are not at work and the bulk viscosity is expected to be negligible. Also, the heat conductivity κ is difficult to determine, since it requires identification of a frame with respect to which heat flows. Any flow of a conserved charge can provide such a frame, so theory has no problems in defining heat conductivity in the Eckart frame of some charge. Experimentally, however, a corresponding operational procedure has not been thought of for heavy-ion collisions. For these reasons, the shear viscosity η_{shear} is the transport coefficient on which the interplay of experiment and theory mainly focuses.

To illustrate the effects of shear viscosity η, we turn again to a simplified model. The model shows Bjorken scaling and has no density or velocity gradients in the transverse plane. So, this is the idealization of a system infinitely extended in the transverse plane. As a consequence, there is no dynamics in the transverse plane, and the system shows for the case of a perfect fluid exactly the dynamics of the 1+1-dimensional toy model described in Eqs. (55)–(63). However, in contrast to a model with only one spatial dimension, shear viscosity does not vanish and one finds

$$\left.\frac{\partial\epsilon}{\partial\tau}\right|_\eta = -\frac{p+\epsilon}{\tau} + \frac{4\eta_{\mathrm{shear}}}{3\tau^2}\,. \tag{78}$$

It is the last term by which this equation of motion differs from that of a perfect fluid, Eq. (62). Using the fundamental thermodynamic relation (61), we find for the entropy density

$$\frac{d(\tau s)}{d\tau} = \frac{\frac{4}{3}\eta_{\mathrm{shear}}}{\tau\,T}\,. \tag{79}$$

We recall that for a perfect fluid with pure one-dimensional Bjorken expansion, the total entropy is $S \propto \tau s$ and it is conserved, $\frac{d(\tau s)}{d\tau} = 0$, see (63). Dissipative corrections lead to entropy increase in the system. This is seen in our example by the non-vanishing right-hand side of (79), and it is generally so.

We may delineate the region of validity of a perfect fluid dynamic description by determining to what extent the entropy increase due to viscous effects is negligible. According to (79), we require

$$\frac{\eta_{\rm shear}}{\tau T}\,\frac{1}{s} \ll 1\,, \qquad \text{if dissipative corrections are negligible.} \tag{80}$$

If we put into this equation a typical temperature scale $T \sim 200$ MeV and a typical time scale $\tau \sim 1$ fm/c, we find $\eta/s \ll 1$. As an aside, we note that the liquid with the lowest shear viscosity over entropy ratio is superfluid helium at 4 K, which has $\eta/s \sim 10$. So, the condition $\eta/s \ll 1$ is a strong constraint on the application of perfect fluid dynamics in heavy-ion collisions. The fact that perfect fluid dynamics appears to provide a phenomenologically valid description of the collisions at RHIC is regarded as a strong indication that the QCD matter produced is exceptionally 'perfect' in the hydrodynamic sense of the word.

We close by commenting on subjects which despite their relevance cannot be covered in these notes. First, the 1st order relativistic fluid dynamics description presented here is known to have deficiencies. In particular, it allows for instantaneous acausal propagation, since the spatial gradient on the right-hand side of (73)–(76) translate instantaneously (and thus outside the light cone) into changes of the dissipative components of the energy–momentum tensor. Whether this conceptual problem is a practical problem depends on the size of the velocity gradients. In a 2nd order relativistic fluid dynamic description, the so-called Israel–Stewart theory, these deficiencies are cured at the price of having to deal with relaxation time constants. Second, we note that the dissipative transport coefficients can be given an exact field theoretic definition in terms of the Green–Kubo formula. This allows for their calculation from first principles of a quantum field theory, a programme which is vigorously being pursued in perturbative finite temperature QCD, in lattice QCD and in a family of supersymmetric theories which share common features with QCD and for which transport coefficients can be calculated with the help of string theory techniques.

Questions:

1. Check that in the Landau frame, the heat flow q^μ in (39) vanishes.
   Answer: In the Landau frame, $q^\mu = \Delta_L^{\mu\alpha}\, T_{\alpha\beta} u_L^\beta$, where the subscript '$L$' indicates that the projector is written in terms of the Landau velocity. Now, $T_{\alpha\beta} u_L^\beta \propto u_L^\alpha$ and hence $q^\mu = 0$.
2. The energy momentum tensor (36) has 10 independent functions. In the Landau frame, $q^\mu(x) = 0$. How are the 10 independent functions of $T^{\mu\nu}$ parametrized in this frame?
   Answer: $\epsilon(x)$ and $p(x)$ are two independent functions. The tracelessness and orthogonality $u_\mu\, \Pi^{\mu\nu} = 0$ of the shear viscous tensor implies that there are five independent functions $\Pi^{\mu\nu}(x)$. In the Landau frame, the remaining three independent functions are not given by the three independent components of q^μ. Rather, the orthogonality condition $q^\mu\, u_\mu = 0$ implies that there are three independent functions $u^\mu(x)$. So, in the Landau frame, $q^\mu(x) = 0$ everywhere, and the three independent functions $q^\mu(x)$ are replaced by three independent functions $u^\mu(x)$.
3. What is the temperature dependence of entropy density for an ideal fluid?
   Answer: Rewrite (61) to obtain $c_s^2 d\epsilon = s\, dT$. Now calculate $d\epsilon/dT$ from (64) to find $s \propto T^{1/c_s^2}$.
4. Show that (60) holds for a 3+1-dimensional perfect fluid with Bjorken boost-invariant initial condition.
   Answer: The lengthy but straightforward calculation can be found in Appendix A of Ref. [12].

5 Hard probes

In heavy-ion collisions at collider energies, there are partonic interactions which occur at high momentum transfer and over small length scale $\Delta x \sim 1/Q$. If this scale is much smaller than the wavelengths of typical excitations in the medium, then one expects on general grounds that the large-Q process is sufficiently pointlike to be unaffected by the medium. However, the partons which enter and leave the hard interaction vertex will propagate through several fermi of dense QCD matter. Thus medium-modification of hard processes can occur via interactions of the partons with the medium in the *incoming* or *outgoing* state. If the hard process can be understood with sufficient precision, then its medium modification can provide information about the medium: the hard process becomes a hard probe.

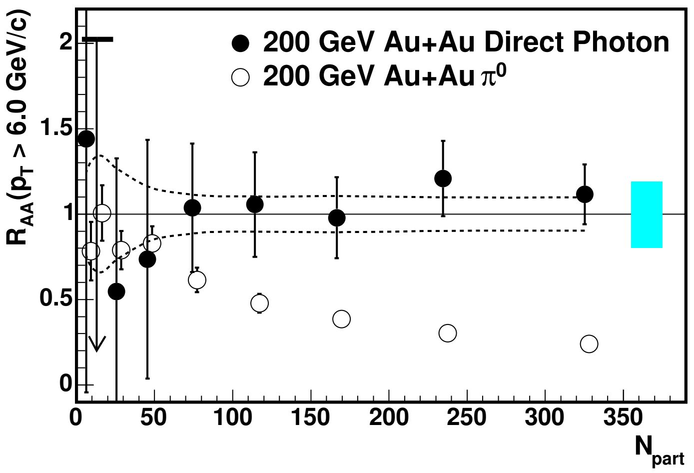

Fig. 8: The nuclear modification factor (82) as a function of centrality given by the number of participants $N_{\rm part}$ for direct photons and neutral pions, measured in $\sqrt{s_{\rm NN}} = 200$ GeV hadronic collisions at RHIC. Particle yields are integrated above $p_T \geq 6$ GeV. The p+p direct photon yield is taken from a next-to-leading order pQCD calculation with scale uncertainty indicated by the shaded bar on the right. Dashed lines indicate the error in determining $\langle N_{\rm coll}^{AB} \rangle$ in (82). All other errors are included in the error bars. Figure taken from Ref. [15].

The picture advocated above assumes that hard processes in heavy-ion collisions can be understood by factorizing the dynamics of the incoming and outgoing partons from that of the hard pointlike partonic interaction. For many hard processes in hadronic (p–p or p–$\bar{p}$) collisions, we know that such a factorization is realized up to corrections of relative order $\sim 1/Q^2$. For the medium-modifications studied in heavy-ion physics, however, factorization is not proven and it is unlikely to hold in the sense of a $1/Q^2$ expansion. To what extent factorization is a useful concept for heavy-ion phenomenology remains to be established in a model-dependent interplay with experiment.

5.1 High-p_T single inclusive hadron spectra in nucleus–nucleus collisions

We shall limit our discussion to one class of hard processes, namely single inclusive hadronic spectra $dN/d^2p_T\, dy$ close to mid rapidity $y \sim 0$ and for sufficiently high transverse momentum p_T. In the absence of medium effects, the high-p_T particle yield grows proportionally to the number of hard partonic interactions, which is proportional to the number of nucleon–nucleon collisions,

$$\frac{dN^{AB\to h}}{d^2p_T\, dy} = \langle N_{\rm coll}^{AB} \rangle \frac{dN^{pp\to h}}{d^2p_T\, dy}\,, \qquad \text{without medium effects.} \tag{81}$$

Here, the average number $\langle N_{\rm coll}^{AB} \rangle$ of nucleon–nucleon collisions is determined by a Glauber model calculation, see Section 2.1.2. The single inclusive spectrum in a nucleon–nucleon collision is determined either experimentally (e.g. in p+p collisions at RHIC or LHC), or theoretically within the framework of perturbative factorization. To characterize deviations from this benchmark, we introduce the nuclear modification factor

$$R_{AB}^h(p_T, y, \text{centrality}) = \frac{\frac{{\rm d}N_{\rm medium}^{AB\to h}}{{\rm d}p_T\,{\rm d}y}}{\langle N_{\rm coll}^{AB} \rangle \frac{{\rm d}N_{\rm vacuum}^{pp\to h}}{{\rm d}p_T\,{\rm d}y}}\,. \tag{82}$$

By construction, this factor equals unity in the absence of medium-effects, and it decreases if the medium suppresses the production of hard particles. Figure 8 shows data for the nuclear modification factor $R_{\rm AA}$ at RHIC. As a measure of the centrality of the collision, this plot uses the number of participants, see our discussion of Fig. 2. With increasing centrality, the high-p_T yield of neutral pions decreases significantly in comparison to the benchmark expectation (81). For the most central collisions, this suppression is approximately 5-fold. In contrast, high-p_T photons appear to be unaffected within errors. This is consistent with the picture that the strong medium-induced suppression of high-p_T hadrons is a final-state effect, which does not occur for photons since these do not interact hadronically. Moreover, if one assumes that high-p_T photon spectra remain unmodified, then the nuclear modification factor for photons becomes a test of the assumption that hard processes in heavy-ion collisions scale with the number of binary nucleon–nucleon collisions, which can be determined via a Glauber calculation of $\langle N_{\rm coll}^{AB}\rangle$.

Figure 8 is but one manifestation of a generic phenomenon. In heavy-ion collisions at RHIC, *all* single inclusive hadron spectra are suppressed by comparable large suppression factors. In particular, one observes:

- Strong and apparently p_T-independent suppression of R_{AA} at high p_T.
  In $\sqrt{s_{NN}} = 200$ GeV, 5–10% central Au–Au collisions at mid-rapidity, one observes a suppression of high-p_T single inclusive hadron yields by a factor $\sim$ 5, corresponding to $R^h_{AuAu}(p_T) \simeq 0.2$ for $p_T \geq$ 5–7 GeV/c. Within experimental errors, this suppression is p_T-independent for higher transverse momenta in all centrality bins.
- Evidence for final-state effect.
  For the most peripheral centrality bin, the nuclear modification factors measured at RHIC are consistent with the absence of medium-effects in both nucleus–nucleus ($R_{AA} \sim 1$) and deuterium–nucleus ($R_{\rm dAu} \sim 1$) collisions. With increasing centrality, R_{AA} decreases monotonically. In contrast, no such suppression is seen in d–Au collisions. These and other observations indicate that the suppression occurs on the level of the produced outgoing partons or hadrons, that it increases with increasing in-medium pathlength in the final state, and that it is hence absent in d–Au collisions, where the in-medium pathlength is negligible.
- Independence of R_{AA} on hadron identity.
  For transverse momenta $p_T \geq$ 5–7 GeV/c, all identified hadron spectra show a quantitatively comparable degree of suppression. There is no particle-species dependence of the suppression pattern at high p_T. Since cross sections for different hadron species differ widely, the species-independence of high-p_T R_{AA} indicates that the mechanism responsible for suppression occurs prior to hadronization.

There are many detailed accounts of these observations in the recent literature, see for instance Ref. [9] and references therein. For the purpose of these notes, we merely observe that the suppression of R_{AA} for hadrons is one of the strongest medium-modifications observed in heavy-ion collisions at RHIC, and that it is a generic phenomenon found in all high-p_T hadron spectra. We also note that the above observations suggest to base a dynamic understanding of this effect on the medium-induced energy loss of high-energy final-state partons prior to hadron formation. As a consequence, the standard modelling of single inclusive hadron spectra proceeds by supplementing a pQCD factorized formalism for single inclusive spectra with a medium modification of the produced partons prior to hadronization in the final state. To explain how this medium modification is introduced, we discuss in the next two sections how the propagation of highly energetic partons is modified in the presence of QCD matter.

5.2 Scattering of highly energetic partons in nuclear matter

The purpose of this subsection is to give for the simplest example a complete derivation of medium-induced gluon radiation of a highly energetic parton traversing a spatially extended target. The case considered is that of an ultra-relativistic quark travelling a long distance through the vacuum (i.e. having the time to build up a fully developed perturbative wave function) prior to impinging on the nuclear target. This problem can be formulated and solved, using quantum-mechanical concepts only. Despite its simplicity, it carries many features of a more complete formulation of radiative energy loss, which we discuss in the next subsection. Here, our discussion follows closely Ref. [16], where more details can be found.

How can we describe the propagation of a highly energetic parton propagating through dense nuclear matter? At high energy, a spatially extended target appears Lorentz contracted, so the propagation time of a partonic projectile through the target is short, partons propagate independently of each other and their transverse positions do not change during the propagation. For the wavefunction Ψ_{in} of an incoming hadronic projectile, the relevant degrees of freedom of each of its partonic components are then the position $\mathbf{x}_i$ in transverse space and the colour index α_i in the fundamental, antifundamental or adjoint representation of the colour $SU(N)$ group, corresponding to a quark, antiquark or gluon in the wave function. We write

$$|\Psi_{in}\rangle = \sum_{\{\alpha_i,\mathbf{x}_i\}} \psi(\{\alpha_i,\mathbf{x}_i\})\, |\{\alpha_i,\mathbf{x}_i\}\rangle\,. \tag{83}$$

In the eikonal approximation applicable at high projectile energy, the only effect of the propagation is that the wave function of each parton in the projectile acquires an eikonal phase due to the interaction with the target field. These phases are given by Wilson lines along the (straight line) trajectories of the propagating particles

$$W(\mathbf{x}_i) = \mathcal{P}\exp\{i\int dz^- T^a A_a^+(\mathbf{x}_i, z^-)\}\,. \tag{84}$$

Here, A^+ is the large component of the target colour field and T^a is the generator of $SU(N)$ in the representation corresponding to a given parton. Equation (84) is the specific form of the phase factor in the light cone gauge $A^- = 0$ for a projectile moving in the negative z direction, so that the light cone coordinate $x^+ = (z+t)/\sqrt{2}$ does not change during propagation through the target. The phase factor takes a different form in other gauges or other Lorentz frames, but the final result is gauge invariant and Lorentz covariant, of course. The projectile emerges from the interaction region with the wave function

$$|\Psi_{out}\rangle = \mathcal{S}\,|\Psi_{in}\rangle = \sum_{\{\alpha_i,\mathbf{x}_i\}} \psi(\{\alpha_i,\mathbf{x}_i\}) \prod_i W(\mathbf{x}_i)_{\alpha_i\beta_i}\, |\{\beta_i,\mathbf{x}_i\}\rangle\,. \tag{85}$$

The phase factors (84) define the scattering matrix $\mathcal{S}$.

The physics implemented in the eikonal formalism is the following: The interaction of the projectile wave function with the target field changes the relative phases between components of the wave function and thus 'decoheres' the initial state. As a result the final-state is different from the initial one, and contains emitted gluons. To see how this works in practice, we consider gluon radiation of a hard quark which propagates at high energy through a nuclear target.

If the quark comes from outside the target, it impinges with a fully developed wave function which contains a cloud of quasi real gluons. In the first order in perturbation theory the incoming wave function contains the Fock state $|\alpha\rangle$ of the bare quark, supplemented by the coherent state of quasi real gluons which build up the Weizsäcker–Williams field $f(\mathbf{x})$,

$$|\Psi^\alpha_{\rm in}\rangle \;=\; |\alpha\rangle + \int d\mathbf{x}\, d\xi\, f(\mathbf{x})\, T^b_{\alpha\,\beta}\, |\beta\,; b(\mathbf{x},\xi)\rangle \tag{86}$$

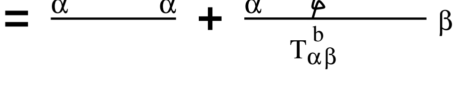

Here Lorentz and spin indices are suppressed. In the projectile light cone gauge $A^- = 0$, the gluon field of the projectile is the Weizsäcker–Williams field

$$A^i(\mathbf{x}) \propto \theta(x^-)\, f_i(\mathbf{x})\,, \qquad\qquad f_i(\mathbf{x}) \propto g\frac{\mathbf{x}_i}{\mathbf{x}^2}\,, \tag{87}$$

where $x^- = 0$ is the light cone coordinate of the quark in the wave function. The integration over the rapidity of the gluon in the wave function (86) goes over the gluon rapidities smaller than that of the quark. In the leading logarithmic order the wave function does not depend on rapidity and we suppress the rapidity label in the following.

The interaction of the projectile (86) with the target leads to a colour rotation $\alpha_i \to \beta_i$ of each projectile component i, resulting in an eikonal phase $W(\mathbf{x}_i)_{\alpha_i\beta_i}$. The outgoing wave function reads

$$|\Psi^\alpha_{\rm out}\rangle \;=\; W^F_{\alpha\gamma}(\mathbf{0})\,|\gamma\rangle + \int d\mathbf{x}\, f(\mathbf{x})\, T^b_{\alpha\beta} W^F_{\beta\gamma}(\mathbf{0})\, W^A_{b\,c}(\mathbf{x})\,|\gamma\,; c(\mathbf{x})\rangle\,, \tag{88}$$

where $W^F(\mathbf{0})$ and $W^A(\mathbf{x})$ are the Wilson lines in the fundamental and adjoint representations respectively, corresponding to the propagating quark at the transverse position $\mathbf{x}_q = \mathbf{0}$ and gluon at $\mathbf{x}_g = \mathbf{x}$.

We want to count the number of gluons in the state (88). If $\Psi_{\rm out}$ lies within the subspace spanned by the incoming states (86), then we have an elastic scattering process in which no gluons are produced. The only gluons in the final-state are then gluons of the gluon cloud of the final-state quark. So, to select those wavefunctions, associated with inelastic processes in which gluons are produced, we have to calculate the projection on the subspace orthogonal to the incoming states,

$$|\delta\Psi_\alpha\rangle = |\Psi^\alpha_{\rm out}\rangle - \sum_\gamma |\Psi_{\rm in}(\gamma)\rangle\langle\Psi_{in}(\gamma)|\Psi^\alpha_{out}\rangle \tag{89}$$

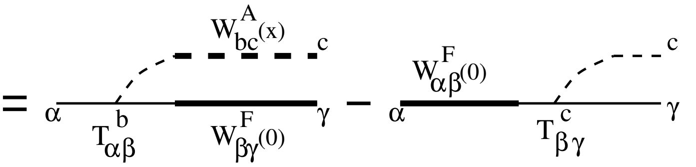

Here, the index γ in the projection operator runs over the quark colour index, so that the second term in (89) projects out the entire Hilbert subspace of incoming states.

The number spectrum of produced gluons is obtained by calculating the number of gluons in the state $\delta\Psi_\alpha$, averaged over the incoming colour index α. After some colour algebra, one obtains

$$\begin{aligned} N_{\rm prod}(\mathbf{k}) &= \frac{1}{N}\sum_\alpha \langle \delta\Psi_\alpha | a^\dagger_d(\mathbf{k})\, a_d(\mathbf{k}) |\, \delta\Psi_\alpha\rangle \\ &= \frac{\alpha_s\, C_F}{2\pi} \int d\mathbf{x}\, d\mathbf{y}\, e^{i\mathbf{k}\cdot(\mathbf{x}-\mathbf{y})} \frac{\mathbf{x}\cdot\mathbf{y}}{\mathbf{x}^2\,\mathbf{y}^2} \Bigg[1 - \frac{1}{N^2-1}\, \langle\langle {\rm Tr}\left[W^{A\dagger}(\mathbf{x})\, W^A(\mathbf{0})\right]\rangle\rangle_t \\ &\qquad - \frac{1}{N^2-1}\, \langle\langle {\rm Tr}\left[W^{A\dagger}(\mathbf{y})\, W^A(\mathbf{0})\right]\rangle\rangle_t \\ &\qquad + \frac{1}{N^2-1}\, \langle\langle {\rm Tr}\left[W^{A\dagger}(\mathbf{y})\, W^A(\mathbf{x})\right]\rangle\rangle_t \Bigg]\,. \end{aligned} \tag{90}$$

Here, we have used $f(\mathbf{x})\, f(\mathbf{y}) = \frac{\alpha_s}{2\pi} \frac{\mathbf{x}\cdot\mathbf{y}}{\mathbf{x}^2\,\mathbf{y}^2}$ for the Weizsäcker–Williams field of the quark projectile in configuration space and the symbol $\langle\langle \dots \rangle\rangle_t$ denotes the averaging over the gluon fields of the target.

It is noteworthy that in the radiation spectrum (90), the entire information about the target resides in the target average of two light-like adjoint Wilson lines. Although the presence of quarks leads to the appearance of fundamental Wilson lines in intermediate stages of the calculation, see e.g. Eq. (88), the averaging involved in (90) combines them into adjoint ones with the help of the Fierz identity $W^F_{ab}(\mathbf{x}) = 2\,{\rm Tr}\left[T^a\, W^{F\dagger}(\mathbf{x}) T^b\, W^F(\mathbf{x})\right]$.

To arrive at an explicit expression for the target average in (90), one needs to specify the target colour field. A particularly simple model is to assume that A^+ arises from a collection of static scattering centres with scattering potentials $a_a^+(\mathbf{q})$ at positions $(\hat{\mathbf{x}}_n, \hat{z}_n)$. In the high-energy approximation, each scattering centre transfers only transverse momentum to the projectile,

$$A_a^+(\mathbf{x}, z^-) = \sum_n \int \frac{d^2\mathbf{q}}{(2\pi)^2} e^{i(\mathbf{x}-\hat{\mathbf{x}}_n)\cdot\mathbf{q}}\, a_a^+(\mathbf{q})\, \delta(z^- - \hat{z}_n^-)\,. \tag{91}$$

The target average can then be defined as an average over the transverse positions of the static scattering centres. Introducing the longitudinal density of scattering centres, $n(z^-) = \sum_n \delta(z^- - \hat{z}_n^-)$, one has

$$\langle\langle \int dz^-\, d\tilde{z}^-\, A_a^+(\mathbf{x}, z^-)\, A_a^+(\mathbf{y}, \tilde{z}^-)\rangle\rangle_t = \int d\xi\, n(\xi)\, \frac{C_A}{2}\, \sigma(\mathbf{x}-\mathbf{y})\,, \tag{92}$$

$$\sigma(\mathbf{x}-\mathbf{y}) = 2\int \frac{d^2\mathbf{q}}{(2\pi)^2} |a^+(\mathbf{q})|^2 \left(1 - e^{i\mathbf{q}\cdot(\mathbf{x}-\mathbf{y})}\right)\,. \tag{93}$$

Here, we have introduced the dipole cross section $\sigma(\mathbf{x}-\mathbf{y})$, which provides in configuration space the full information about the cross section $|a^+(\mathbf{q})|^2$ of a single scattering centre. The target average of two Wilson lines can then be defined in terms of this dipole cross section

$$\frac{1}{N^2-1}\langle\langle \mathrm{Tr}\left[W^{A\dagger}(\mathbf{y})\, W^A(\mathbf{x})\right]\rangle\rangle_t \approx \exp\left[-\frac{C_A}{4\, C_F}\int d\xi\, n(\xi)\, \sigma(\mathbf{x}-\mathbf{y})\right]\,. \tag{94}$$

5.3 Gluon radiation off quarks produced in the medium

The purpose of this subsection is to discuss medium-induced gluon radiation off a parton produced in a large momentum transfer process *in the medium.* This problem is significantly more complicated than that discussed in the previous section mainly because of two issues:

- Interference between radiation in the vacuum and medium-induced radiation
  In the absence of a medium, a parton produced in a hard process will radiate its large virtuality Q on a typical timescale $1/Q$ by developing a parton shower. In the rest frame of the medium, this time scale is Lorentz dilated by a factor E_{parton}/M, where the parton mass is $M \sim Q$. Typical radiation times $\sim E_{\mathrm{parton}}/Q^2$ are comparable to the typical in-medium pathlengths in a nucleus–nucleus collision. As a consequence, one expects an interference pattern between the radiation present in the vacuum, and the additional radiation induced due to scattering in the medium.
- Corrections to eikonal approximation are needed
  In the ultra-high-energy (eikonal) approximation, the longitudinal extension of the target is contracted to a delta function. As a consequence, gluon radiation off a hard parton occurs either before or after the target, but not within the target. This can be seen e.g. in Eq. (89), where the Wilson lines (which stand for interactions between projectile and target) occur in both diagrams only before or after the gluon radiation vertex. In contrast, to take interference effects into account, it is important to locate the gluon emission vertex inside the medium. This requires a formulation which knows about longitudinal distances in the medium. The momentum conjugate to longitudinal distance is the light cone energy p_-. So, to place an emission vertex within the medium, one has to keep track at least of the $1/p^-$ corrections to the eikonal formalism.

In the following, we present the main elements of a formulation which goes beyond the eikonal approximation and accounts for interference effects between vacuum and medium-induced radiation. We start by writing down a light-cone Green's function

$$G(\mathbf{r}_{\mathrm{in}}, x_{\mathrm{in}}^-; \mathbf{r}_{\mathrm{out}}, x_{\mathrm{out}}^- | p^-) = \int_{\mathbf{r}(x_{\mathrm{in}}^-)=\mathbf{r}_{\mathrm{in}}}^{\mathbf{r}(x_{\mathrm{out}}^-)=\mathbf{r}_{\mathrm{out}}} \mathcal{D}\mathbf{r}(\xi)\, \exp\left[i\frac{p^-}{4}\int_{x_{\mathrm{in}}^-}^{x_{\mathrm{out}}^-} d\xi\, \dot{\mathbf{r}}^2(\xi)\right]\, W(\mathbf{r}(\xi); x_{\mathrm{in}}^-, x_{\mathrm{out}}^-)\,, \tag{95}$$

$$W(\mathbf{r}; x^-_{\rm in}, x^-_{\rm out}) = \mathcal{P}\, \exp\left[i \int_{x^-_{\rm in}}^{x^-_{\rm ou}} d\xi\, A^+(\mathbf{r}(\xi), \xi) \right] \,. \tag{96}$$

Equation (95) is the solution of the Dirac equation for a coloured partonic projectile propagating in a spatially extended colour field A^+. The solution is exact up to order $O(1/p^-)$. To this order, it contains a non-eikonal Wilson line (96), which ‘wiggles’ in transverse position along a path $\mathbf{r}(\xi)$. In the limit of ultra-high parton energy, $p^- \to \infty$, when the finite energy corrections of order $O(1/p^-)$ vanish, this expression reduces to the eikonal Wilson line (84),

$$\lim_{p^- \to \infty} G(\mathbf{r}_{\rm in}, x^-_{\rm in}; \mathbf{r}_{\rm out}, x^-_{\rm out} | p^-) = W(\mathbf{r}_{\rm in}; x^-_{\rm in}, x^-_{\rm out})\, \delta^{(2)}(\mathbf{r}_{\rm out} - \mathbf{r}_{\rm in}) \,. \tag{97}$$

In close analogy to the target averages in the eikonal formalism [see Eqs.(92)–(94)], one finds that the target averages over pairs of Green’s functions (95) of energy αp and $(1-\alpha)p$ leads to a path integral expression

$$\mathcal{K}(\mathbf{r}', z'; \mathbf{r}, z | \mu) \quad = \quad \int \mathcal{D}\mathbf{r}\, \exp\left[i \int\limits_{z}^{z'} d\xi\, \left[\frac{\mu}{2} \dot{\mathbf{r}}^2 + i\, \frac{1}{2} n(\xi)\, \sigma\left(\mathbf{r}\right) \right] \right] \,. \tag{98}$$

Here, $\mu \equiv \alpha(1-\alpha)p$. Also, in accordance with the notation used in parton energy loss calculations, we have changed from light-cone coordinates to the longitudinal z, and we have absorbed a factor C_A/C_F in the definition of the dipole cross section. Keeping these notational changes in mind, one can check that the $\mu \to \infty$ limit of (98) coincides with the average (94) of two eikonal Wilson lines, as it should.

The inclusive energy distribution of gluon radiation off an in-medium produced parton can be expressed in terms of the Zakharov path integral (98) like

$$\begin{aligned} \omega \frac{dI}{d\omega} \quad &= \quad \frac{\alpha_s\, C_R}{(2\pi)^2\, \omega^2}\, 2{\rm Re} \int_{\xi_0}^{\infty} dy_l \int_{y_l}^{\infty} d\bar{y}_l \int d\mathbf{u} \int_0^{\chi\omega} d\mathbf{k}_\perp\, e^{-i\mathbf{k}_\perp \cdot \mathbf{u}}\, e^{-\frac{1}{2} \int_{\bar{y}_l}^{\infty} d\xi\, n(\xi)\, \sigma(\mathbf{u})} \\ &\times \frac{\partial}{\partial \mathbf{y}} \cdot \frac{\partial}{\partial \mathbf{u}} \int_{\mathbf{y}=0}^{\mathbf{u}=\mathbf{r}(\bar{y}_l)} \mathcal{D}\mathbf{r}\, \exp\left[i \int_{y_l}^{\bar{y}_l} d\xi \frac{\omega}{2} \left(\dot{\mathbf{r}}^2 - \frac{n(\xi) \sigma\left(\mathbf{r}\right)}{i\, \omega} \right) \right] \,. \end{aligned} \tag{99}$$

Here, $\mathbf{k}_\perp$ denotes the transverse momentum of the emitted gluon. The two-dimensional transverse coordinates $\mathbf{u}$, $\mathbf{y}$ and $\mathbf{r}$ emerge in the derivation of (99) as distances between the positions of projectile components in the amplitude and complex conjugate amplitude. The longitudinal coordinates y_l, $\bar{y}_l$ integrate over the ordered longitudinal gluon emission points in amplitude and complex conjugate amplitude. The limit $k_\perp = |\mathbf{k}_\perp| < \chi\, \omega$ on the transverse phase space restricts gluon emission to a finite opening angle Θ, $\chi = \sin\Theta$. For the full angular integrated quantity, $\chi = 1$.

Equation (99) is a compact expression. Its derivation and full explanation lie outside the scope of these lectures. Here, we limit ourselves to a discussion of the main physics features encoded in (99). We observe first that all information about the medium enters again via the dipole cross-section times density, as in the eikonal formalism (94). While the expression (99) has been derived for a particular model (91) of the target field strength, Eq. (94) suggests a more model-independent interpretation: the only medium-dependent information entering the gluon energy distribution (99) is information about the target expectation value of an adjoint Wilson loop whose long side points in the light-like direction. In fact, what matters mainly is the short transverse distance behaviour of this Wilson loop. At short distances, we can write

$$n(\xi)\, \sigma(\mathbf{r}) \simeq \frac{1}{2}\, \hat{q}(\xi)\, \mathbf{r}^2 \,. \tag{100}$$

Here, $\hat{q}(\xi)$ is refered to as BDMPS (Baier–Dokshitzer–Mueller–Peigné–Schiff) transport coefficient. As first exploited by Zakharov, using (100) in the energy distribution (99) amounts to a saddle point approximation of the path integral. The path integral becomes that of a harmonic oscillator and can be calculated explicitly.

Figure 9 shows a numerical evaluation of the medium-induced gluon energy distribution (99) for a static BDMPS transport coefficient $\hat{q} = \hat{q}(\xi)$ extending over a finite in-medium pathlength L.

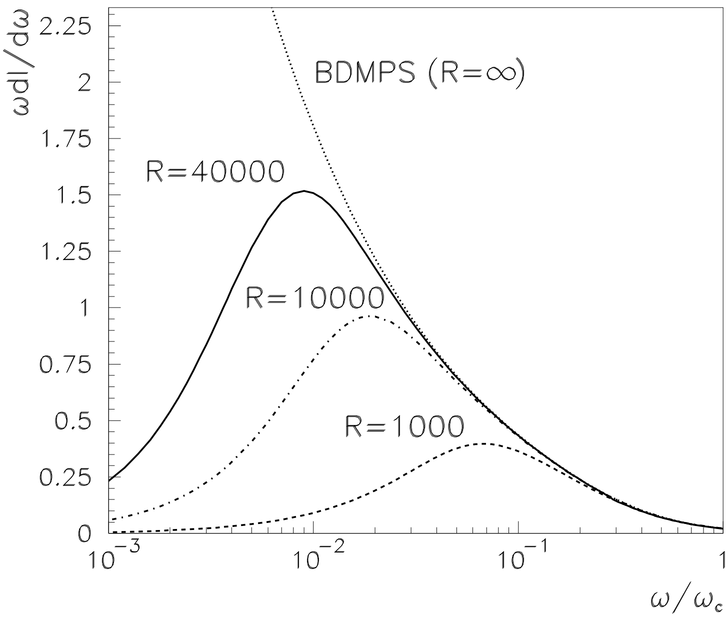

Fig. 9: The medium-induced gluon energy distribution $\omega \frac{dI}{d\omega}$ as a function of the gluon energy ω in units of $\omega_c = \frac{1}{2}\hat{q}\, L^2$, and for different values of the kinematic constraint $R = \omega_c\, L$. Figure taken from Ref. [17].

Main features of the gluon energy distribution in Fig. 9 can be understood in terms of qualitative arguments. We consider a gluon in the hard parton wave function. This gluon is emitted due to multiple scattering if it picks up sufficient transverse momentum to decohere from the partonic projectile. For this, the average phase φ accumulated by the gluon should be of order one,

$$\varphi = \left\langle \frac{k_\perp^2}{2\omega}\, \Delta z \right\rangle \sim \frac{\hat{q}\, L}{2\omega} L = \frac{\omega_c}{\omega}\,. \tag{101}$$

Thus, for a hard parton traversing a finite path length L in the medium, the scale of the radiated energy distribution is set by the 'characteristic gluon frequency"

$$\omega_c = \frac{1}{2}\, \hat{q}\, L^2\,. \tag{102}$$

For an estimate of the shape of the energy distribution, we consider the number $N_{\rm coh}$ of scattering centres which add coherently in the gluon phase (101), $k_\perp^2 \simeq N_{\rm coh}\, \langle q_\perp^2 \rangle_{\rm med}$. Based on expressions for the coherence time of the emitted gluon, $t_{\rm coh} \simeq \frac{\omega}{k_\perp^2} \simeq \sqrt{\frac{\omega}{\hat{q}}}$ and $N_{\rm coh} = \frac{t_{\rm coh}}{\lambda} = \sqrt{\frac{\omega}{\langle q_\perp^2 \rangle_{\rm med}\, \lambda}}$, one estimates for the gluon energy spectrum per unit path length

$$\omega \frac{dI}{d\omega\, dz} \simeq \frac{1}{N_{\rm coh}}\, \omega \frac{dI^{1\,\rm scatt}}{d\omega\, dz} \simeq \frac{\alpha_s}{t_{\rm coh}} \simeq \alpha_s \sqrt{\frac{\hat{q}}{\omega}}\,. \tag{103}$$

This $1/\sqrt{\omega}$-energy dependence of the medium-induced non-Abelian gluon energy spectrum is expected for sufficiently small $\omega < \omega_c$. It is confirmed in Fig. 9 if one neglects (as for the above estimate) kinematical constraint in transverse phase space, which cut off the energy distribution in the infrared. For the ω-integrated average parton energy loss, one finds analytically from (99)

$$\langle \Delta E \rangle_{R\to\infty} = \lim_{R\to\infty} \int_0^\infty d\omega\, \omega \frac{dI}{d\omega} = \frac{\alpha_s C_R}{2}\, \omega_c \propto \hat{q}\, L^2 \,. \tag{104}$$

The same parametric dependence $\propto \hat{q}\, L^2$ can be found from the above pocket estimates, if one integrates the differential distribution (103) over an in-medium path length L and over the gluon energy ω up to ω_c, above which (103) breaks down since the phase φ is smaller than unity. So, the pocket estimate (103) provides the correct small-ω behaviour as well as the correct dependence of the average energy loss on density and in-medium path length. In particular, the L^2-dependence was first derived by BDMPS.

5.4 Comparing parton energy loss calculations to data

Models including radiative parton energy loss have been shown to reproduce the main qualitative and quantitative features of high-p_T hadron spectra at RHIC. In the simplest case, one uses the standard pQCD factorized formalism for the calculation of single inclusive hadron spectra in p–p. This defines the denominator of the nuclear modification factor (82). For the calculation of the same spectrum in nucleus–nucleus collisions, one then specifies a model in which the transverse momentum of the outgoing partons is degraded as a function of the in-medium path length and of properties of the medium (such as its local density). For instance, the BDMPS parton energy loss discussed in the previous section leads to a model description, in which this final-state parton energy loss depends on the BDMPS quenching parameter $\hat{q}$ and the geometry of the collision. Figure 10 shows but one example that models of radiative parton energy loss can reproduce main features in the data if the only model parameter $\hat{q}$ is chosen appropriately.

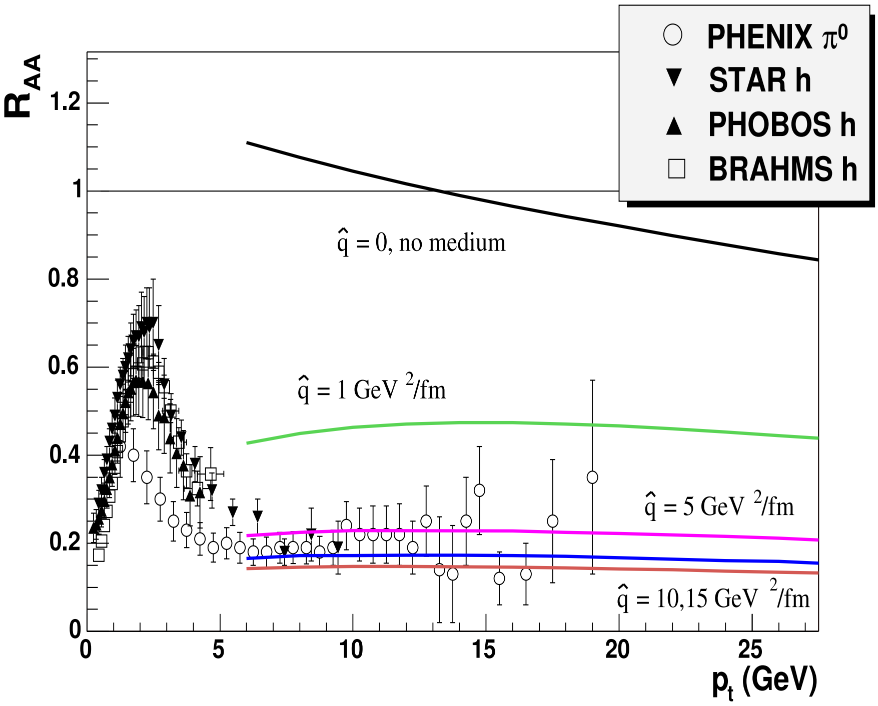

Fig. 10: The nuclear modification factor $R_{AA}(p_T)$ for charged hadrons and neutral pions in central Au+Au collisions at 200 A GeV, together with curves from a model of radiative parton energy loss [18] for different quenching parameter $\hat{q}$

A critical review of the state of the art in such data comparison lies beyond the scope of these lecture notes. It would have to include a detailed discussion of alternative descriptions of parton energy loss, additional nuclear effects (such as initial-state p_T-broadening), trigger biases in different measurements, issues of nuclear geometry and expansion of the collision region, etc. All these issues are problems of current research. Rather than elaborating on them, we conclude these lecture notes with a list of some of the many questions which are currently under investigation and are likely to play a role at the LHC:

1. What is the microscopic mechanism underlying high-p_T hadron suppression at RHIC?
   The above discussion assumed that radiative parton energy loss causes hadron suppression. There are arguments supporting a dominant role of radiative parton energy loss. But the question to what extent other possible sources of parton energy loss (e.g. collisional mechanisms) can be discriminated is not settled.
2. How does parton energy loss depend on parton identity?
   Radiative energy loss models predict a hierarchy of suppression patterns: gluons lose more energy than light quarks, and light quarks lose more energy than heavy quarks. But the quantitative question above which p_T-scale this should be seen clearly in the nuclear modification factor and how it will be reflected in the particle species dependence of R_{AA} is not fully clarified. Also, the possible role of other parton energy loss mechanisms is still unclear.
3. How does parton energy loss establish itstelf in jet-like correlations and jets?
   This question encompasses a wide range of open problems which become particularly relevant at the LHC. First, it is a topic of intense current investigation as to how jets are modified beyond the leading hadron due to the presence of dense QCD matter. Second, the question arises which characteristics of a jet can be identified unambiguously in the high multiplicity environment of a heavy-ion collision.
4. ......
   This list could be much longer. There are many questions which have not yet been sufficiently explored, and there may be many relevant question which have not even been asked properly. The common feature of all these questions is that they should be asked within a theory which we know well (QCD), but they are asked in a novel regime of high density where we do not yet know how this theory functions. Use your chance to work on such questions!

Questions:

1. Calculate explicitly the projection $|\delta\Psi_\alpha\rangle$ in (89) of the wavefunction $|\Psi^\alpha_{\rm out}\rangle$ (88) on the subspace orthogonal to the incoming states.
   Answer: The result has the structure given diagrammatically in (89). Details about the derivation can be found in Ref. [16].
2. From the explicit expression for $|\delta\Psi_\alpha\rangle$ in (89) derive the number of produced gluons (90).

Acknowledgements

It is my pleasure to thank the organizers and students of the CERN schools in Vina del Mar and in Trest for their efforts in making these schools a memorable experience. My special thanks go to Rolf Baier and Paul Romatschke who helped me in ways too numerous to enumerate to improve on a series of lectures that I gave in 2005 at the University of Bielefeld, and that are part of the backbone of these notes.

References

[1] D. Kharzeev and M. Nardi, Phys. Lett. B **507** (2001) 121 [arXiv:nucl-th/0012025].

[2] C. W. De Jager, H. De Vries and C. De Vries, Atom. Data Nucl. Data Tabl. **14** (1974) 479.

[3] A. Bialas, M. Bleszynski and W. Czyz, Nucl. Phys. B **111** (1976) 461.

[4] J. Adams *et al.* [STAR Collaboration], Phys. Rev. Lett. **91** (2003) 072304 [arXiv:nucl-ex/0306024].

[5] A. J. Kuhlman and U. W. Heinz, Phys. Rev. C **72** (2005) 037901 [arXiv:nucl-th/0506088].

[6] K. J. Eskola, Nucl. Phys. A **698** (2002) 78 [arXiv:hep-ph/0104058].

[7] N. Armesto and C. Pajares, Int. J. Mod. Phys. A **15** (2000) 2019 [arXiv:hep-ph/0002163].

[8] W. Busza, Acta Phys. Polon. B **35**, 2873 (2004) [arXiv:nucl-ex/0410035].

[9] N. Borghini and U. A. Wiedemann, arXiv:0707.0564 [hep-ph].

[10] N. Borghini, P. M. Dinh and J. Y. Ollitrault, Phys. Rev. C **63** (2001) 054906 [arXiv:nucl-th/0007063].

[11] J. Adams *et al.* [STAR Collaboration], Phys. Rev. C **72** (2005) 014904 [arXiv:nucl-ex/0409033].

[12] P. F. Kolb, J. Sollfrank and U. W. Heinz, Phys. Rev. C **62** (2000) 054909 [arXiv:hep-ph/0006129].

[13] P. F. Kolb and U. W. Heinz, arXiv:nucl-th/0305084.

[14] U. W. Heinz, arXiv:nucl-th/0512051.

[15] S. S. Adler *et al.* [PHENIX Collaboration], Phys. Rev. Lett. **94** (2005) 232301 [arXiv:nucl-ex/0503003].

[16] A. Kovner and U. A. Wiedemann, arXiv:hep-ph/0304151.

[17] C. A. Salgado and U. A. Wiedemann, Phys. Rev. D **68**, 014008 (2003) [arXiv:hep-ph/0302184].

[18] K. J. Eskola, H. Honkanen, C. A. Salgado and U. A. Wiedemann, Nucl. Phys. A **747** (2005) 511 [arXiv:hep-ph/0406319].